Single-cell characterization of human GBM reveals regional differences in tumor-infiltrating leukocyte activation

Philip Schmassmann[1,*], Julien Roux[2,3], Steffen Dettling[4], Sabrina Hogan[1], Tala Shekarian[1], Tomás A. Martins[1], Marie-Françoise Ritz[1], Sylvia Herter[5], Marina Bacac[5], and Gregor Hutter[1,6,*]

[1]Brain Tumor Immunotherapy Lab, Department of Biomedicine, University of Basel, Basel, Switzerland

[2]Bioinformatics Core Facility, Department of Biomedicine, University of Basel, Basel, Switzerland

[3]Swiss Institute of Bioinformatics, Basel, Switzerland

[4]Roche Pharmaceutical Research and Early Development, Roche Innovation Center Munich, Penzberg, Germany

[5]Roche Pharmaceutical Research and Early Development, Roche Innovation Center Zürich, Schlieren, Switzerland

[6]Department of Neurosurgery, University Hospital Basel, Basel, Switzerland

[*]Correspondence: p.schmassmann@unibas.ch, gregor.hutter@usb.ch

Abstract

Glioblastoma (GBM) harbors a highly immunosuppressive tumor microenvironment (TME) which influences glioma growth. Major efforts have been undertaken to describe the TME on a single-cell level. However, human data on regional differences within the TME remain scarce. Here, we performed high-depth single-cell RNA sequencing (scRNAseq) on paired biopsies from the tumor center, peripheral infiltration zone and blood of five primary GBM patients. Through analysis of > 45'000 cells, we revealed a regionally distinct transcription profile of microglia (MG) and monocyte-derived macrophages (MdMs) and an impaired activation signature in the tumor-peripheral cytotoxic-cell compartment. Comparing tumor-infiltrating $CD8^+$ T cells with circulating cells identified $CX3CR1^{high}$ and $CX3CR1^{int}$ $CD8^+$ T cells with effector and memory phenotype, respectively, enriched in blood but absent in the TME. Tumor $CD8^+$ T cells displayed a tissue-resident memory phenotype with dysfunctional features. Our analysis provides a large-scale dissection of GBM-associated leukocytes, serving as a reference map of human GBM-TME.

Introduction

Glioblastoma (GBM) is a fatal disease without effective long-term treatment options. The current standard of care consists of tumor resection followed by adjuvant chemoradiotherapy resulting in a median overall survival of only 14 months [1]. One of the hallmarks in GBM progression is the high rate of neovascularization. The GBM-induced aberrant vessels not only nourish glioma cells, but also provide a specialized niche for tumor-associated stromal and immune cells such as monocyte-derived macrophages (MdMs), yolk sac-derived microglia (MG) (together termed glioma-associated macrophages/microglia, GAMs), and peripheral adaptive immune cells. This immune tumor microenvironment (iTME) paradoxically acts in an immunosuppressive manner and promotes tumor progression [2]. For example, clinical trials of systemic T cell checkpoint blockade showed only disappointing results [3, 4], which was attributed in part to the immunosuppressive components of the GBM iTME. The origin of GAMs, infiltration of peripherally derived macrophages across the blood-brain-barrier (BBB) or recruitment of tissue-resident MG to the tumor site, as well as their contribution to gliomagenesis are studied intensively [2, 5-7]. Hence, major efforts have been undertaken to describe the GBM iTME on a single cell level [5, 6, 8]. However, human data on the composition of the iTME in different tumor regions (contrast enhancing tumor center versus peripheral infiltration zone) remain scarce [9, 10].

To study the region-dependent cellular diversity within individual GBMs, we performed single-cell RNA sequencing (scRNA-seq) on patient-matched biopsies from the tumor center and the peripheral infiltration zone of five primary GBM patients. Additionally, peripheral blood mononuclear cells (PBMC) of the same patients were included to explore the transcriptional changes occurring during tumor infiltration of circulating immune cells.

Our analysis revealed a regionally distinct transcription profile of MG and MdMs and an impaired activation signature in the tumor-peripheral cytotoxic-cell compartment. Comparing tumor-infiltrating $CD8^+$ T cells with PBMC-derived, identified $CX3CR1^{high}$ and $CX3CR1^{int}$ $CD8^+$ T cells with effector and memory phenotype, respectively, enriched in blood but absent in the iTME. Tumor $CD8^+$ T cells displayed features of tissue-resident memory T cells and were characterized by an exhaustion phenotype. This work provides a large-scale dissection of glioma-associated cell types complemented by patient-matched PBMCs, revealing an abundance of information about the composition and molecular diversity of the iTME in GBM.

Results

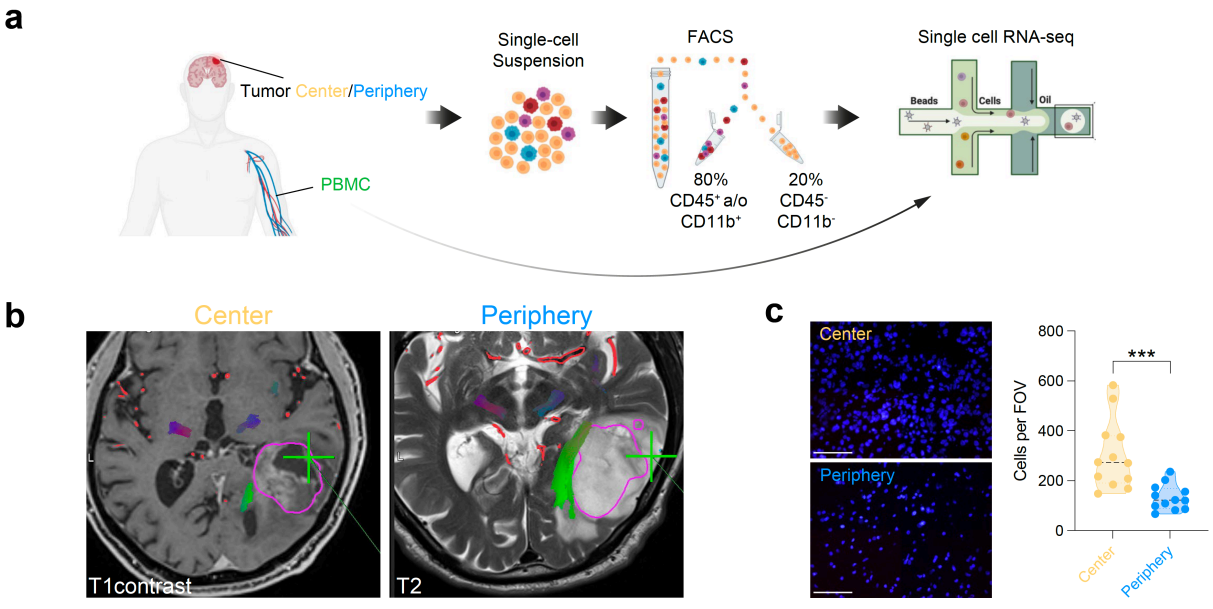

Fig. 1 Single-cell RNA-seq of cells from tumor center, periphery and blood. a Experimental workflow for single-cell analysis of cells isolated from tumor center, periphery and peripheral blood mononuclear cells (PBMC), including fluorescent-activated cell sorting and 3'-scRNA-seq. **b** Axial T1 with contrast (left) and T2 (right) MRI brain in a patient with a left temporal GBM. Fresh tumor biopsies were taken according to neuronavigation (green cross). The tumor center was defined as contrast enhancing, whereas the tumor periphery was defined as T2 hyperintense. **c** Nuclear DAPI staining of resected tissue specimens. 40x magnification (scale bar = 20 µm). n = 3 patients, 4 field of view (FOV) per patient. Statistics: ***$p < 0.001$, two-tailed Mann Whitney U test.

scRNA-seq analysis of paired tumor center, periphery and PBMC samples.

Fresh, neurosurgically resected tissue from five GBM patients were harvested (Supplementary Table 1). According to the 2021 WHO Classification of Tumors of the Central Nervous System [11], in which the term glioblastoma designates only IDH-wildtype grade 4 tumors, we will hence use the term grade 4 glioma, as we included as well IDH-mutant grade 4 tumors (Supplementary Table 1). The tumor center was defined as contrast enhancing, whereas the tumor periphery was defined as T2 hyperintense by magnetic resonance imaging (MRI)-guided, navigated surgical resection (Fig. 1b). Increased cellular density of the center vs. periphery samples was confirmed by nuclear DAPI staining on matched histological micrographs of the resected tissue specimens used for scRNA-seq (Fig. 1c). As outlined in Fig. 1a, we separately processed patient tumor and blood samples and enriched them for immune cells by fluorescence-activated cell sorting (FACS) (Supplementary Fig. 1a and 1b). The three samples per

patient (center, periphery and PBMC) were loaded on different wells of a 10x Genomics Chromium system for a targeted recovery of 10,000 cells. Due to technical issues cells from the center sample of patient BTB 609 could not be collected.

In total we analyzed 45,466 cells that passed initial quality control and filtering, comprising 8,254 cells from tumor center, 5,954 cells from tumor periphery and 31,258 PBMCs, with 6,354 to 10,957 cells per patient (Supplementary Table 2; Supplementary Fig. 1c-1f). All cells were projected onto a two dimensions *t*-distributed stochastic neighbor embedding (tSNE) [12]. As we observed a good overlap of cells across patients, we chose not to perform any correction for patient-specific effects (Supplementary Fig. 1g). Using hierarchical clustering, the cells were partitioned into clusters (Supplementary Fig. 3a) which were then annotated into eight distinct cell types for the immune subset and five cell types for the CD45 negative subset (Fig. 2a; Supplementary Fig. 3b, g-h; Supplementary Table 2). Notably: the annotation of most of the immune cell types was performed by whole-transcriptome comparison of our cells to a reference dataset of bulk RNA-seq samples of sorted immune cell types from human PBMC (Supplementary Fig. 3c) [13]; the annotation of MdMs and microglia was performed by whole-transcriptome comparison to a dataset of bulk RNA-seq samples of sorted immune cell types from the tumor microenvironment of human gliomas (Supplementary Fig. 3d) [5] and using signature scores defined from scRNA-seq of GAMs (Supplementary Fig. 3e-f) [7]; finally, CD45 negative cells were annotated by whole-transcriptome comparison to a scRNA-seq dataset of *IDH1*^{wt} GBM (Supplementary Fig. 3i) [14]. The expression of known marker genes across cell types is shown in Fig. 2b, and genes whose expression is most specific to each cell type are shown in Supplementary Fig. 2.

In line with previous work [5, 6, 10], we noted that GAMs accounted for the most frequent cell type in the center iTME (on average 44.5% among leukocytes in center vs. 24.7% among leukocytes in periphery), while the T cell compartment accounted for the most abundant immune population in the tumor periphery (Fig. 2d). When comparing phagocytic cell types, we found that MdMs decreased substantially in the glioma periphery, while MG did not exhibit a differential distribution between tumor center and periphery (Fig. 2e).

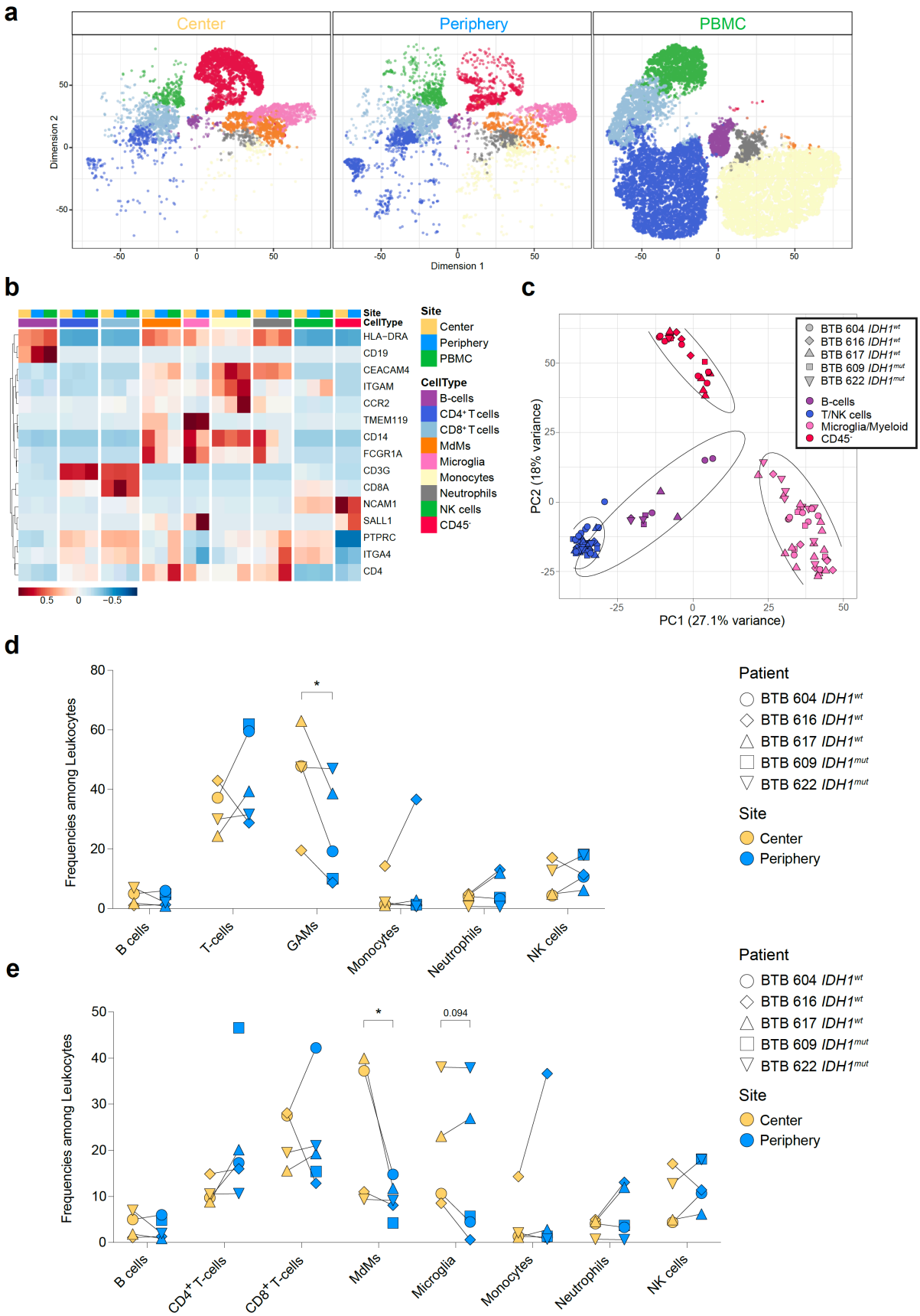

Fig. 2 Single-cell RNA-seq analysis identifies main immune cell populations. a Dimensionally reduced tSNE projection of the scRNAseq data showing the identified main cell clusters. **b** Heatmap displaying averaged and normalized expression values of characteristic cell-type

specific genes used to annotate clusters in (**a**). Columns are ordered by site and cell type, and rows show centered and scaled expression values, hierarchically clustered. **c** Principal component (PC) biplot of pseudo-bulk scRNAseq samples aggregated by patient and cell type. Symbols represent individual patients and cell lineage is displayed by different colors. **d, e** Relative frequencies of immune populations among leukocytes between tumor center and periphery. Symbols represent individual patients and paired samples are indicated by connecting lines. Statistics: *FDR<5%, *diffcyt-DA-voom* method.

MG and MdMs display regionally distinct transcription profiles.

To perform a differential expression analysis between tumor sites, we stratified the analysis by annotated cell type and aggregated cells from each patient (see Supplementary Methods). A principal component analysis (PCA) on the aggregated transcriptome data confirmed that the major source of variation was the cell type lineage (Fig. 2c), with notable differences between lymphoid, MG/myeloid cells, and $CD45^-$ cells (PCs 1 and 2). Interestingly there was no clear association between patient *IDH1* status and these or deeper components, suggesting that the iTME seemed independent of *IDH1* status in grade 4 glioma. Moreover, immune cell type differential abundance analysis revealed an equal distribution among *IDH* variants, further supporting this observation (Fig. 2d, e).

Differential expression analysis between MG from tumor center and periphery revealed a highly significant downregulation of inflammatory genes in the peripheral MG. This included scavenger receptors (*CD36* and *MARCO*), chemokines (*CXCL3* and *CCL20*) and immune receptors (*IL7R [15]* and *CD109*, a negative regulator of TGF-β signaling [16]) as well as genes involved in cell growth (*CSRP1*) and cell metabolism (*SMPDL3A [17]* and *SDS*) (Fig. 3a and Supplementary Table 3). The latter transcribes for the serine dehydratase, an enzyme catalyzing the dehydration of L-serine/L-threonine to yield pyruvate/ketobutyrate [18]. The downregulation of *SDS* in the peripheral MG with reduced metabolization of L-serine to pyruvate could potentially lead to a reduced oxidative phosphorylation in peripheral MG, a metabolic feature described for dysfunctional MG in Alzheimer's disease models [19]. Concomitantly, increased L-serine levels have been associated with the induction of alternative, M2-like microglial polarization and inhibited secretion of inflammatory factors (TNF-α and IL-1β) [20].

Interestingly, we found upregulation of Inhibitor of DNA-Binding 1, also known as Inhibitor of Differentiation 1 (*ID1*) in the peripheral MG, which is well described in GBM progression, treatment resistance and glioma stem cell biology [21]. Recently, new evidence has emerged, linking *ID1* to suppression of the anti-tumor immune response in the myeloid compartment and promoting tumor progression [22].

To further explore the underlying biological processes differing between MG in the two compartments, we conducted a gene set enrichment analysis (GSEA) on the results of the differential expression analysis using Gene Ontology (GO) database (Biological Processes). This revealed overall a significant downregulation of GO categories involved in antigen processing and presentation via MHC-I and MHC-II in the peripheral MG relative to the center MG, as well as downregulation of amino acid metabolism and TNF-α signaling pathway (Fig. 3b),

which further supported our observation of a strong immunosuppressive phenotype in peripheral MG.

When comparing the transcriptional profile of MdMs from the peripheral front to the tumor center, we observed upregulation of proinflammatory genes *MEFV* encoding pyrin [23] and *APOBEC3A,* a cytidine deaminase involved in RNA editing during macrophage M1 polarization and response to interferons (IFN) [24]. Moreover, upregulation of *KCNJ2*, a voltage-dependent potassium channel has been shown to regulate macrophage proliferation [25] whereas *GPR132* serves as lactate sensor in the acidic TME and could potentially facilitate MdM migration to the tumor site [26]. *MIR22HG*, a long non-coding RNA (lncRNA) has been associated with tumor suppressive properties in hepatocellular carcinoma, where it has been linked to chemokine signaling pathways and phagosome activation [27] (Fig. 3c).

Along with this, we observed downregulation of anti-inflammatory genes in the peripheral MdMs. This included *RNASE1*, a signature gene of macrophages enriched in immune checkpoint inhibitor (ICI) non-responding melanoma patients [28], *PLTP*, a negative regulator of NF-κB activation [29], *NRP1*, a key gene required for macrophage attraction towards hypoxic tumor niches and thereby retaining their pro-tumorigenic features [30], and *IL4I1*, a novel metabolic immune checkpoint in the tryptophan/aryl hydrocarbon receptor (AHR) pathway [31] (Fig. 3c). Hence, MdMs might display a proinflammatory phenotype in the glioma periphery, however, are less abundant there (Fig. 2e).

We observed a marked downregulation of *SDS* in the peripheral MdMs, similar to the peripheral MG population, leading to a presumptive accumulation of L-serine in the peripheral MdMs. In contrast to MG, serine metabolism has been shown to indeed support proinflammatory IL-1β cytokine production in macrophages [32]. Together with the reduced tryptophan metabolism through *IL4I1* and downregulated *SLC39A8*, a transmembrane zinc importer whose reduction has been linked to increased IL-6/IL-1β secretion and increased NF-κB signaling in innate immunity [33], these data shed new light on regional differences in the innate immunometabolism in the iTME of grade 4 glioma.

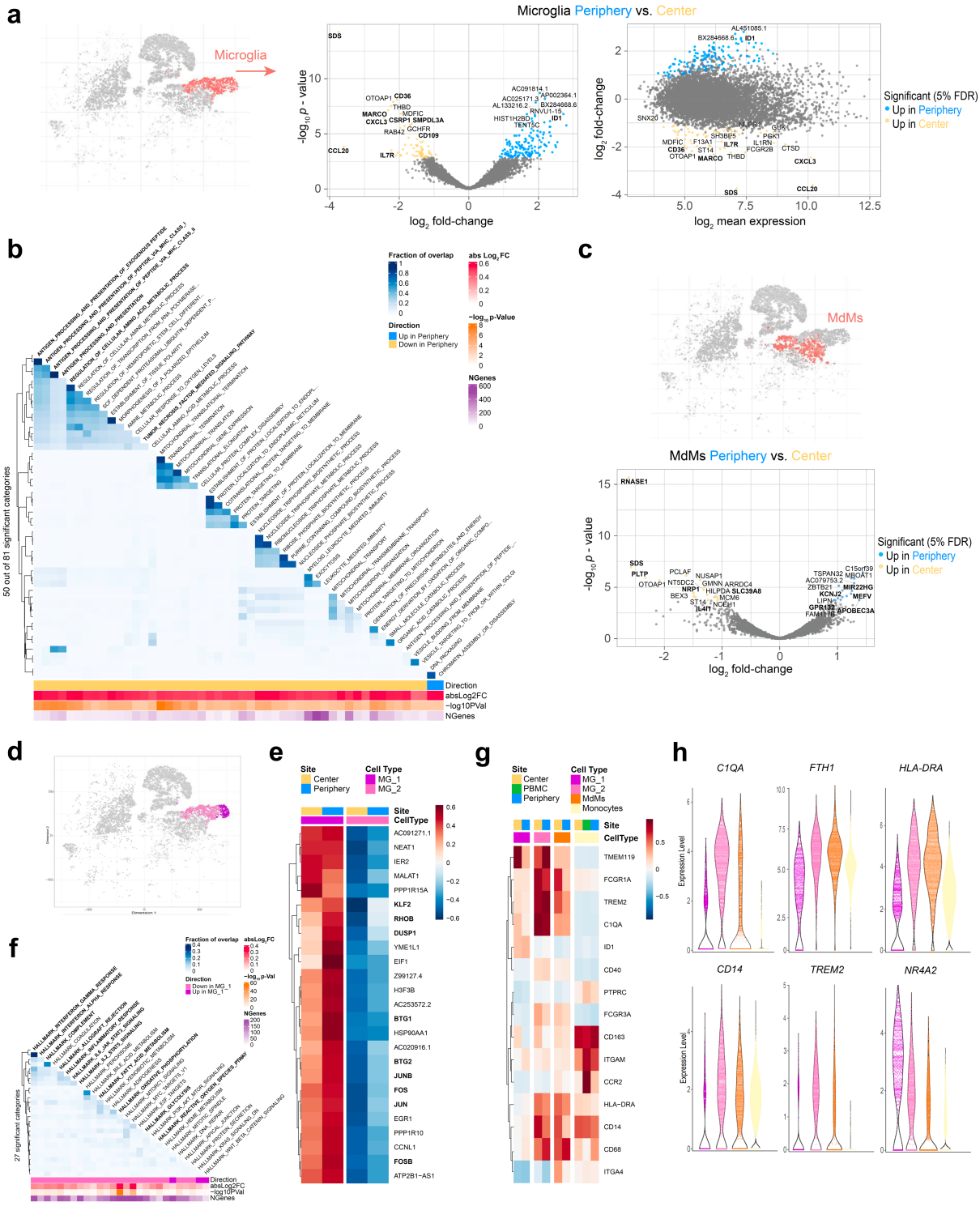

Fig. 3 MG and MdMs display distinct regional transcription profiles. a Microglia cluster highlighted on tSNE map and scatterplots showing differentially expressed genes (FDR<5%, indicated by blue and yellow) in Microglia (MG) cells from tumor periphery versus center. Volcano plot showing *p* value versus fold-change (left) and MA plot showing fold-change versus mean expression (right). **b** Heatmap representation of Gene set enrichment analysis (GSEA) results between peripheral and center microglia using Gene Ontology (GO) collection (Biological Processes). The fraction of overlap between gene sets is calculated as Jaccard coefficient

of overlap between the gene sets. **c** Monocyte-derived macrophages (MdMs) cluster highlighted on tSNE map and volcano plot showing statistical significance (FDR<5%, indicated by blue and yellow) versus fold-change of differentially expressed genes in MdMs from tumor periphery versus tumor center. **d** Unsupervised hierarchical sub-clustering of the MG population revealed two transcriptionally distinct subsets of MG, termed MG_1 and MG_2, displayed on the tSNE map. **e** Heatmap displaying the cluster-specific genes identifying MG_1 and MG_2 subclusters. Columns are ordered by site and cell type, and rows show centered and scaled expression values, hierarchically clustered. **f** Heatmap representation of GSEA between MG_1 and MG_2 subclusters using Hallmark collection of major biological categories. **g** Heatmap displaying previously described reactivity markers of MG. Columns are ordered by site and cell type, and rows show centered and scaled expression values, hierarchically clustered. **h** Violin plot showing expression levels of selected reactivity markers among mononuclear phagocyte populations.

The iTME of grade 4 glioma harbors two transcriptionally distinct MG subpopulations.

Unsupervised hierarchical sub-clustering of the MG population revealed two transcriptionally distinct iTME MG subsets, which we termed MG_1 and MG_2, respectively (Fig. 3d and 3e). The MG_1 cluster was highly enriched for the activator protein-1 (AP-1) family of transcription factors including *FOS, FOSB, JUN, JUNB, MAF* and *MAFB* (Fig. 3e and Supplementary Table 4), which convey a surveilling phenotype to adult MG, but are also involved in numerous processes including cell growth, differentiation and immune activation [34]. Specifically, *FOSB* gene products have been implicated in the excitotoxic MG activation by regulating complement C5a receptor expression [35]. Yet, concomitant upregulation of anti-inflammatory Krüppel-like factor 2 (*KLF2*) [36] and Dual Specificity Protein Phosphatase 1 (*DUSP1*), an inhibitor of innate inflammation by negatively regulating the mitogen-activated protein kinase (MAPK) pathway [37], together with increased expression of anti-proliferative genes like *RHOB, BTG1* and *BTG2* paint a more complex picture of these cells. Particularly, *BTG1* has been identified as an activation-induced apoptotic sensitizer in MG after exposure to inflammatory stimuli [38], serving as an autoregulatory mechanism and possibly hinting towards an exhausted state in these MG_1 cells. GSEA for differences between MG_1 and MG_2 clusters using the MSigDB Hallmark collection of major biological pathways [39] revealed downregulation of many MG effector functions in the MG_1 population including (1) inflammation ("Complement", "Inflammatory Response", "Allograft Rejection", "Reactive Oxygen Species Pathway"), (2) immune cell activation ("IFN-α Response", "IFN-γ Response", "IL6 JAK STAT3 Signaling", "IL2 STAT5 Signaling") and (3) immunometabolism ("Fatty Acid Metabolism", Oxidative Phosphorylation", "Glycolysis") (Fig. 3f). As we examined the expression of previously described reactivity markers of MG including *C1QA,* Ferritin (*FTH1*), *FCGR1A, HLA-DRA, CD14* and *TREM2 [40-43],* and established MG homeostatic genes like *CX3CR1, HEXB* and *SPI1* (PU.1), we noted a marked downregulation of these genes in the MG_1 cluster, while the anti-inflammatory transcription factors *NR4A2* [44] and *NR4A1* [45] were highly upregulated (Fig. 3g, 3h, Supplementary Fig. 4a and Supplementary Table 4). Additionally, while total MG didn't show differences in abundance between tumor sites (Figure 2e), changes could be observed when stratifying for MG subclusters. We noted in 3 of 4 (75%) paired center-periphery samples an increased abundance of MG_1 cells in the tumor periphery. And, the presumably more reactive MG_2 cells concomitantly decreased significantly in frequency in the tumor periphery (Supplementary Fig. 4b). Collectively, these data argue for the non-reactive/exhausted phenotype of MG_1.

The tumor peripheral cytotoxic cell compartment exhibits an impaired activation signature.

Next, we investigated the regional differences in the lymphoid compartment composed of $CD4^+$ and $CD8^+$ T cells and natural killer (NK) cells. We observed only very few significant changes in the transcriptomic profiles of $CD4^+$ T cells between tumor center and periphery (Supplementary Fig. 4c and Supplementary Table 3). Yet, comparing peripheral $CD8^+$ T cells with $CD8^+$ T cells from tumor center revealed 110 differentially expressed genes (43 genes upregulated and 67 genes downregulated) (Fig. 4a and Supplementary Table 3). Many down-regulated genes in the peripheral $CD8^+$ T cells associated with canonical IFN responses (*IFI6, IFI27, MX1, STAT1, EPSTI1 PARP9, ISG15)* [46] cell proliferation (*STMN1, CENPF, HELLS, NUSAP1* and *DNPH1*) and T cell co-stimulation (*CD28, TMIGD2* (CD28H), *TNFRSF4* (OX40), *CD27* and *TNFRSF18* (GITR)) (Fig. 4a). Contrary to our expectations, we saw upregulation of *CTLA4* in the center $CD8^+$ T cells which acts as a negative costimulatory molecule. However, unlike other costimulatory receptors, such as CD27 and CD28, CTLA-4 is not constitutively expressed on T lymphocytes [47]. but only induced following T cell activation, along with positive costimulatory molecules such as OX40 and GITR. In addition, upregulation of CTLA-4 requires entry into the cell cycle [47]. In line with that, we detected an upregulation of proliferative genes in center $CD8^+$ T cells. In summary, CTLA-4 induction in center $CD8^+$ T cells rather suggested T cell activation than exhaustion, especially since other inhibitory receptors like *PDCD1* (PD-1), *LAG3* and *HAVCR2* (TIM-3) were not differentially expressed between sites. Moreover, we did not observe differential expression of genes involved in $CD8^+$ T cell effector functions like cytotoxicity (e.g., *GZMK, GZMB, KLRG1,* PRF1) or cytokines (e.g., *CCL5, XCL1, XCL2, IL10*). Yet, we noted upregulation of inhibitory genes (*TGFB1* and *FCRL6* [48]) in the peripheral $CD8^+$ T cells, suggesting that a pool of activated, proliferating and IFN-responsive $CD8^+$ T cells is present in the tumor center, but fails to populate the infiltrative tumor periphery.

Similar trends were observed for the peripheral NK cell population with peripherally reduced IFN response (*MX1* and *IFI44L*), and proliferative genes (*STMN1, HELLS, CENPF, PTTG1* and *DNPH1*), downregulated stimulatory receptors (*TMIGD2* (CD28H) and *TNFRSF18* (GITR)), and reduced NF-κB signaling (*NFKB1* and *RELB*) (Fig. 4b and Supplementary Table 3). Although, we observed upregulation of key genes associated with NK cell effector function in the periphery (e.g., *FCGR3A* (CD16), *FGFBP2, ITGB2, GZMH* and *KIR2DS4*), increased expression of inhibitory receptors like *LILRB1* and *KLRG1*, the latter especially in co-expression with chemokine receptor *CX3CR1*, identified the peripheral NK cells rather to be terminally differentiated with impaired cytotoxic capabilities [49]. This was in line

with the observed abrogated cytokine activity profile in the peripheral NK cells with reduced expression of key factors like *XCL1, XCL2, LTB* and *CKLF*. In summary, our data revealed an impaired activation signature in the peripheral cytotoxic cell compartment.

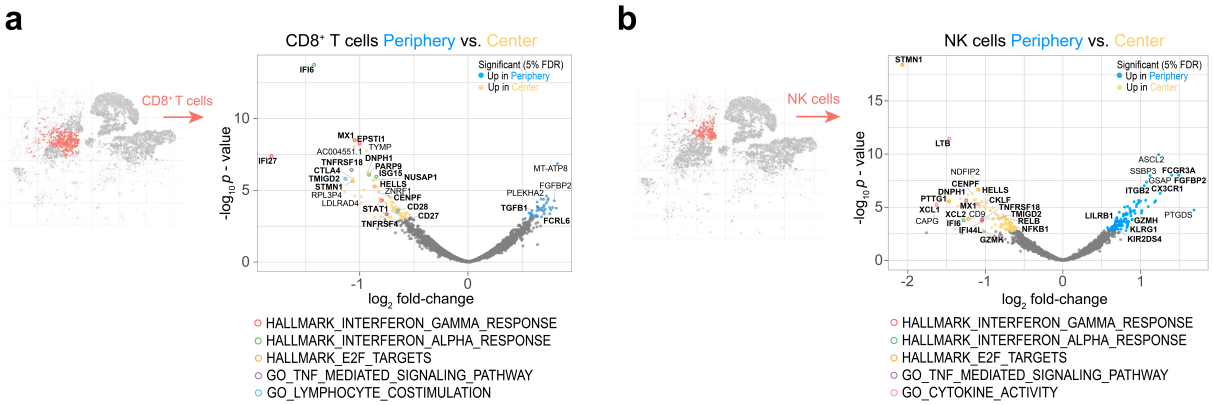

Fig. 4 The peripheral cytotoxic cell compartment exhibits an impaired activation signature. a, b Volcano plots showing differentially expressed genes (FDR corrected p value < 0.05, indicated by blue and yellow) in CD8$^+$ T cells (**a**) and NK cells (**b**) from tumor periphery versus tumor center. Colored rings mark genes belonging to selected GSEA Hallmark or Gene Ontology (GO) pathways as indicated.

CX3CR1 labels a specific CD8$^+$ T cell population in the circulation of grade 4 glioma patients.

Next, we investigated the relationships between circulating CD8$^+$ T cells and those from the tumor milieu and, more specifically, the peripheral, infiltration zone characterized by an abrogated CD8$^+$ T-cell IFN response and activation signature. Strikingly, there were large transcriptomic differences between PBMC and periphery CD8$^+$ T cells (Fig. 5a), with 1,417 differentially expressed genes (864 genes upregulated in the tumor periphery and 553 genes upregulated in PBMC) (Fig. 5b, Supplementary Table 5).

Interestingly, one of the key genes upregulated in PBMC CD8$^+$ T cells was the chemokine receptor *CX3CR1*, whose expression labelled a specific population among these cells (Fig. 5c). Flow cytometry of an additional matched glioma grade 4 patient cohort confirmed an increased abundance of CX3CR1$^+$ CD8$^+$ T cells in PBMC compared to almost absent CX3CR1$^+$ CD8$^+$ T cells in tumor periphery (Fig. 5d, Supplementary Table 1).

Recently, expression of CX3CR1 was demonstrated to distinguish memory CD8$^+$ T cells with cytotoxic effector function [50]. Further characterization of classical central memory (T_{cm}) and effector memory (T_{em}) populations by varying surface expression levels of CX3CR1 identified a novel CX3CR1^{int} subpopulation, termed peripheral memory (T_{pm}). T_{pm} cells underwent frequent homeostatic divisions, re-acquired CD62L, homed to lymph nodes, and predominantly surveyed peripheral tissues compared to T_{cm} and T_{em} [51]. In our dataset, the circulating CX3CR1$^+$ CD8$^+$ T cells indeed displayed a core signature of memory CD8$^+$ T cells with effector function, comprising expression of LFA-1 (*IGAL- ITGB2*), *EOMES, SELL* (CD62L), *CCR7^{low}, CD27^{low}, TBX21^{high}* (Tbet), *IL7R, TCF7, FAS* and *ITGB1,* separating them from circulating *CX3CR1$^-$ CD28^{high}*, *CD27^{high}* and *IL7R^{high}* naive CD8$^+$ T cells (Fig. 5e and Supplementary Fig. 5b). The observed high expression of cytolytic molecules *GZMB* (Granzyme B) and *PRF1* (Perforin 1) in the *CX3CR1$^+$* cells advocated for their cytotoxic effector phenotype (Fig. 5n). Flow cytometric analysis confirmed T_{eff} to be CX3CR1^{high}, with negligible expression levels in the naive CD8$^+$ T cells, whereas the identified memory CD8$^+$ T cells (T_{em} and T_{pm}) were CX3CR1^{int} (Fig. 5f, 5g). Collectively, surface expression analysis of CX3CR1 identified a subset of CX3CR1^{high} T_{eff} and CX3CR1^{int} memory (T_{em}, T_{pm}) CD8$^+$ T cells in the circulation of grade 4 glioma patients with potentially elevated tissue surveilling properties in the case of T_{pm}, which are, however, largely absent in the tumor microenvironment.

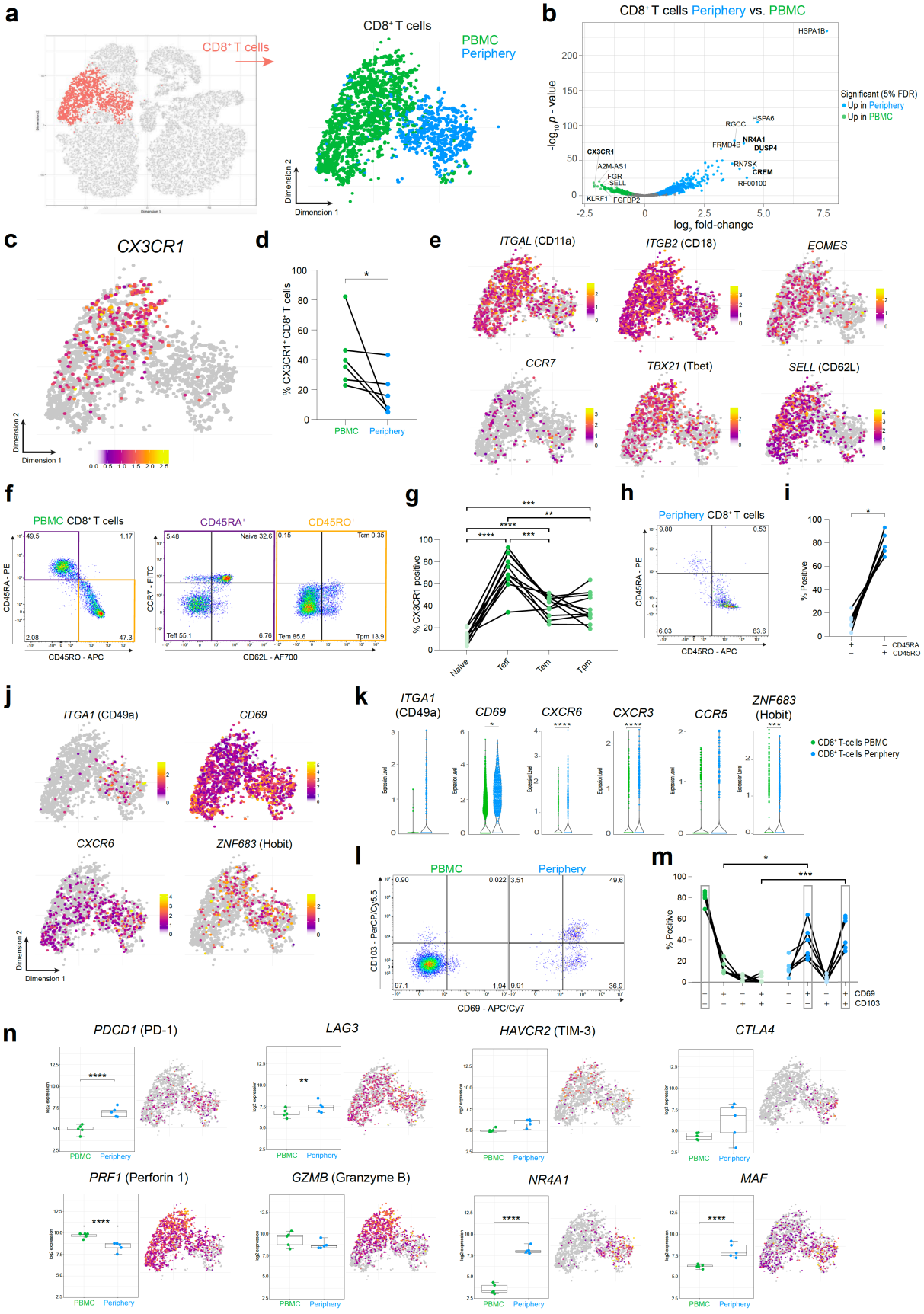

Fig. 5 CD8⁺ T cells in grade 4 glioma show distinct memory phenotypes depending on site. **a** CD8⁺ T cell cluster highlighted on tSNE map (left). CD8⁺ T cell cluster colored by site of origin (right). **b** Volcano plot showing differentially expressed genes (FDR corrected *p* value <

0.05, indicated by blue and green) in $CD8^+$ T cells from tumor-periphery versus PBMC. **c** Expression of *CX3CR1* overlaid on tSNE $CD8^+$ T cell cluster. **d** Frequency of $CX3CR1^+$ $CD8^+$ T cells among all $CD8^+$ T cells in flow cytometry data. **e** Expression of genes associated with memory (upper row) and effector memory (lower row) phenotype overlaid on tSNE $CD8^+$ T cell cluster. **f** Gating procedure applied to identify $CD3^+$ $CD8^+$ naive, T effector cells (T_{eff}), effector memory (T_{em}), peripheral memory (T_{pm}) and central memory (T_{cm}), eluted from PBMCs. **g** Expression of CX3CR1 in $CD8^+$ T cell subpopulations identified in (**f**). **h** Representative dot plot of tumor-periphery $CD8^+$ T cells stained for CD45RA and CD45RO. **i** Quantification of tumor-periphery $CD8^+$ T cells expressing CD45RA or CD45RO. **j** Expression of genes associated with tissue-resident memory (T_{rm}) phenotype overlaid on tSNE $CD8^+$ T cell cluster. **k** Average expression levels of selected T_{rm} markers between $CD8^+$ T cells from PBMC versus tumor-periphery. **l** Representative dot plots of CD69 and CD103 co-expression in $CD8^+$ T cells from PBMC and tumor-periphery. **m** Quantification of CD69 and CD103 co-expression revealed $CD69^-$ $CD103^-$ in PBMC and $CD69^+$ $CD103^-$ and $CD69^+$ $CD103^+$ in tumor-periphery as the dominant phenotypes. **n** Expression of selected markers associated with T cell exhaustion/dysfunction, shown as boxplots between $CD8^+$ T cell from PBMC and tumor-periphery and overlaid on tSNE $CD8^+$ T cell cluster. $n = 6$ donors (**d, i, m**), $n = 11$ donors (**g**). Statistics: Wilcoxon matched-pairs signed rank test (**d, i**); repeated measures one-way ANOVA with post-hoc Šidák's correction for multiple comparisons (**g, m**). For detailed statistical analysis of scRNA-seq expression data, please refer to supplementary methods section. $*p \leq 0.05$, $**p \leq 0.01$, $***p \leq 0.001$, $****p \leq 0.0001$, no brackets indicate no significant difference.

$CD8^+$ T cells in the tumor periphery share features with tissue-resident memory T cells (T_{rm})

We next examined the differing transcriptional and surface-specific features between tumor infiltrating and circulating $CD8^+$ T cells. Surface staining for CD45RA and CD45RO, discriminating naive/effector from memory T cells, attributed a predominant $CD45RO^+$ memory phenotype to the tumor infiltrating $CD8^+$ T cells (Fig. 5h, 5i). Interrogation of the transcriptomic profile of these cells revealed a key marker expression signature consistent with tissue-resident memory T cells (T_{rm}): Expression of cellular adhesion molecules (integrins) *ITGA1* (CD49a) and *ITGAE* (CD103), tissue retention marker *CD69*, chemokine receptors implicated in tissue-homing *CXCR3, CXCR6* and *CCR5* [52] and transcription factors, *ZNF683* (Hobit) and *PRDM1* (Blimp1) as well as reduced expression of *TBX21* (Tbet) and *EOMES* [53], strongly suggested a T_{rm} phenotype for these cells (Fig. 5j, 5k and Supplementary Fig. 5b). Co-expression analysis of paired PBMC and tumor periphery samples using flow cytometry showed that $CD69^+$ $CD103^-$ and $CD69^+$ $CD103^+$ cells are the dominant $CD8^+$ T cell populations in the tumor periphery (Fig. 5l and 5m). Combined, these data strongly suggest a T_{rm} phenotype for the $CD8^+$ T cells in the tumor periphery.

Previous reports of T_{rm} populating the brain in the aftermath of central or peripheral infections concluded that brain T_{rm} cells surveil the brain tissue and mediate protection by rapid activation and enhanced cytokine production [52]. Indeed, $CD8^+$ T cells in the tumor periphery showed increased expression of genes belonging to costimulatory pathways, including *ICOS, TNFRSF4* (OX40) and *TNFRSF9* (4-1BB) (Supplementary Fig. 5c, Supplementary Table 5), albeit accompanied by high levels of inhibitory receptors *PDCD1* (PD-1), *LAG3, HAVCR2* (TIM-3) and *CTLA4* (Fig. 5n). Moreover, expression of genes coding for cytotoxic molecules, including Granzyme B and Perforin 1 were decreased in the peripheral $CD8^+$ T cells, suggesting a compromised killing capacity of these cells. And lastly, $CD8^+$ T cells in the tumor periphery exhibited a transcription factor profile of exhausted T cells with high expression of *NR4A1, MAF* and *IRF4* (Fig. 5n and Supplementary Fig. 5d), which have been implicated in T cell dysfunction and exhaustion [54, 55]. Collectively, these data indicate that $CD8^+$ T cells in the glioma periphery share features with T_{rm} cells. However, inhibitory receptor expression, functional molecules and transcriptional signature ascribe an exhausted phenotype to these cells.

Noteworthy, we observed high upregulation of similar genes in the comparison tumor periphery vs. PBMC for $CD4^+$ T cells as for $CD8^+$ T cells (Fig. 5b and Supplementary Fig. 5e). These included transcription factor family *NRA41-3,* identified as key mediator of T cell dysfunction [55], Dual Specificity Protein Phosphatase 2/4 (*DUSP2, DUSP4*) described as negative regulators of mitogen-activated protein (MAP) kinase superfamily and associated with

impaired T cell effector activity [56] and T cell senescence [57], and transcription factor *CREM* which has been implicated in IL-2 suppression [58]. These genes could potentially identify pan T cell dysfunction markers within the GBM iTME [59].

Interrogation of cell-cell interactions revealed critical role of SPP1-mediated crosstalk between MG and lymphocytes in the tumor periphery

We next investigated cell-cell interactions based on ligand-receptor expression levels using the CellChat platform [60]. Considering MG being on average the main innate immune population in the tumor periphery (Fig. 2e), and lymphocytes displaying an impaired activation signature, we focused our analysis on the tumor-peripheral crosstalk between MG and lymphocytes (Fig. 6a). This revealed SPP1 (Osteopontin) as a leading potential cell-cell interaction mediator between MG and lymphocytes (Fig. 6a and 6b). MG SPP1-mediated signaling was as well among the most significant interactions, when investigating cell-cell communication across all cell types and both sites (Supplementary Fig. 6a and 6b). Further, we found that *SPP1* is mainly expressed by MG rather than glioma cells, contrary to previous reports [61] (Fig. 6c, Supplementary Fig.6c and 6d). MG SPP1 conveys different interactions, depending on the recipient cell binding receptor expression profile. NK cells could interact with SPP1 mainly via the integrin complex *ITGA4-ITGB1* (CD49d-CD29) (Fig. 6c), mediating NK cell adhesion and migration [62]. This might facilitate interaction of inhibitory NK receptors KLRB1 and CD94/NKG2A with MG C-type lectin-related ligands and HLA-E, respectively, which could explain the observed impaired activation state of peripheral NK cells.

$CD4^+$ and $CD8^+$ T cells exhibited strong interactions with MG *SPP1* as well (Fig. 6b). However, cell-cell communication between MG and T lymphocytes could be mainly mediated via SPP1/CD44 interaction (Fig. 6a and 6c), a ligand-receptor axis recently described to suppress T cell activation and proliferation [63]. Altogether, cell-cell interaction analysis pointed towards an impaired activation signature in the peripheral glioma-associated immune cells and revealed potentially involved signaling pathways.

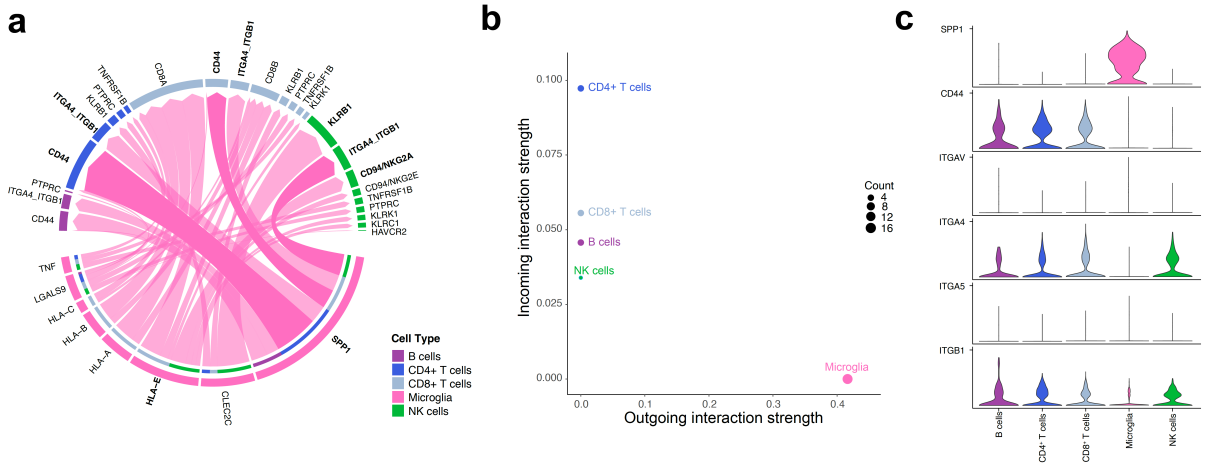

Fig. 6 Cell-cell communication analysis using CellChat reveals critical role for SPP1-mediated crosstalk in tumor periphery. a Chord diagram showing significant interactions from microglia to lymphocyte cell clusters. The inner bar colors represent the targets that receive signal from the corresponding outer bar. The inner bar size is proportional to the signal strength received by the targets. Chords indicate ligand-receptor pairs mediating interaction between two cell clusters, size of chords is proportional to signal strength of the given ligand-receptor pair. **b** Comparison of incoming and outgoing interaction strength allows identification of main senders and receivers. **c** Violin plots showing the expression distribution of signaling genes involved in the inferred SPP1 signaling network.

Discussion

In this study, we combined single-cell RNA sequencing and flow cytometry-based proteome analysis to interrogate the regional leukocyte activation signature in patient-matched biopsies from contrast-enhancing tumor center, infiltrative peripheral rim, and blood PBMCs of grade 4 glioma patients. Our analyses revealed a distinct, regionally dependent transcriptional profile for most of the investigated cell populations. While peripheral MG and cytotoxic cells predominantly displayed an impaired activation signature, MdMs showed pro-inflammatory traits in the tumor periphery, however, were less abundant there compared to the tumor center, which was reported by others as well [9, 10]. Supplemented with transcriptional and surface proteome analysis of paired PBMC samples, we provide an in-depth characterization of the three main immunological compartments of grade 4 glioma.

Previous studies focused on the description of the TME of grade 4 glioma, which also considered regional differences, yet they focused primarily at neoplastic cells rather than the immune compartment [9]. Others investigated the differences in the iTME composition between primary and metastatic brain tumors [5, 6]. Interestingly, the two latter ones reported differences in the iTME composition between *IDH1*^{wt} and *IDH1*^{mut} glioma, which we did not observe in our transcriptional data. Of note, both authors included low-grade and even pre-treated recurrent glioma patients into the *IDH1*^{mut} group, representing a quite heterogenous patient cohort. In this study, we aimed at providing a representative selection of primary, treatment-naive grade 4 glioma patients including *IDH1*^{wt} and *IDH1*^{mut}. Surprisingly, we only found negligible transcriptional iTME differences among these two groups.

We identified a transcriptionally distinct MG subcluster, MG_1, which displayed an anti-inflammatory/non-reactive phenotype. A similar MG subpopulation expressing a comparable gene signature has been recently described to be enriched in Alzheimer's disease patients [64]. Additionally, the peripheral cytotoxic cell compartment exhibited an impaired activation state, including a downregulated IFN response signature in CD8$^+$ T cells. Induction of an IFN response state has been described as a consequence of T cell receptor-mediated IFN-γ production, likely serving as an autocrine response and inducing the proliferative program [46]. Hence, the reduced autocrine IFN-responsive state in the tumor peripheral CD8$^+$ T cells, together with downregulated proliferative and co-stimulatory genes emphasized their impaired activation in the peripheral infiltration zone.

By exploring the transcriptional trajectory of CD8$^+$ T cells from the blood circulation into the immunosuppressive TME of the tumor periphery, we uncovered CX3CR1^{high} and CX3CR1^{int} effector and memory CD8$^+$ T cells, respectively, to be highly enriched in the PBMC,

but absent in the iTME. Recently, adoptive transfer studies of CX3CR1$^+$ CD8$^+$ T cells in a melanoma mouse model significantly suppressed tumor growth [65]. Others identified increased frequencies of CX3CR1$^+$ CD8$^+$ T cells in non-small cell lung and melanoma patients who responded to anti-PD-1 therapy, where these cells exhibited migratory capabilities into the tumor site followed by potent tumor rejection [65, 66]. Thus, the authors proposed T cell CX3CR1 expression as a predictor of response to ICI therapy. Therefore, the absence of ICI therapy-responsive CD8$^+$ T cells in the glioma TME could additionally explain the disappointing outcomes of clinical trials using ICI in glioma patients.

The observed T_{rm} exhaustion phenotype of the glioma residing CD8$^+$ T cells was recently reported as well for tumor-infiltrating PD-1^{high} CD8$^+$ T cells in hepatocellular carcinoma [54]. Whether these glioma-associated CD8$^+$ T cells really possess tumor-specificity requires further study. Particularly in the light of a recent study by Smolders and colleagues who reported a consistent brain-resident CD8$^+$ T cell population in a miscellaneous autopsy cohort of patients with neurological disorders excluding brain malignancies (Alzheimer's disease, Parkinson's disease, dementia, depression, multiple sclerosis), as well as patients with no known brain disease. These brain-resident CD8$^+$ T cells displayed a remarkably consistent T_{rm} phenotype [67]. The authors further showed high expression of inhibitory receptors CTLA-4 and PD-1 on the brain-resident CD8$^+$ T_{rm} cells, which is in line with the core phenotypic signature of T_{rm} cells from other tissues [68, 69]. Yet, the brain CD8$^+$ T_{rm} cells showed a preserved inflammatory potential with substantial production of IFN-γ and TNF-α upon *ex vivo* stimulation. They concluded that extensive immune activation with release of highly neurotoxic lytic enzymes, such as perforin and granzyme B, harmfully impacts the brain parenchyma and should be tightly controlled, whilst maintaining the capability to elicit a fast inflammatory response when a neurotropic virus threatens the CNS [67]. Therefore, inhibitory receptors like PD-1 and CTLA-4 on brain CD8$^+$ T_{rm} cells may support CNS homeostasis by preventing uncontrolled T cell reactivity, and the availability of the receptor ligands may determine their inhibitory effect. While this may represent a well-balanced equilibrium under healthy conditions, the tumor setting leads to its disruption with upregulation of inhibitory ligands like PD-L1 on glioma cells and CD86 on GAMs, leading to the dysfunctional state seen in the glioma-residing CD8$^+$ T_{rm} cells.

Another study comprehensively showed, that peripheral infections generate antigen-specific CD8$^+$ T_{rm} cells in the brain, mediating protection against CNS infections [52]. These data could implicate that the glioma-associated CD8$^+$ T cells are devoid of tumor-specific reactivity, but rather represent a pre-existing T cell population generated after peripheral infections,

481 which acquired a dysfunctional state upon glioma formation. To test this hypothesis, further
482 characterization of these cells is required, including analysis of T cell receptor clonality and
483 tumor-specificity by patient-matched T cell/glioma-sphere co-culture assays.

484 Lastly, our cell-cell interaction analysis revealed signaling pathways between peripheral
485 MG and lymphocytes potentially inducing the observed impaired activation signature. In fact,
486 interaction of NK cell receptor *KLRB1* (CD161) with its C-type lectin-related ligand has been
487 identified lately as a candidate inhibitory receptor on glioma-infiltrating T cells [70] and
488 SPP1/CD44 interaction has been described to suppress T cell activation and proliferation [63].

489 Limitations of the study include the limited patient number, thereby our study was nei-
490 ther designed nor powered to explore differences in neoplastic cells, given the high inter- and
491 intra-patient variability in glioma cells [9]. Importantly, our dataset establishes a starting point
492 for further interrogation and provides an in-depth analysis of the transcriptional landscape of
493 the major immune populations in grade 4 glioma within three important regional compartments.
494 Further, we confirmed the observed phenotype of $CD8^+$ T cells in the blood and tumor periphery
495 by flow cytometry in a cohort of ten additional patients, addressing possible generalization
496 concerns. Together, we provide a novel reference map of leukocyte activation in the TME and
497 blood circulation from grade 4 glioma patients, helping the research community to uncover
498 novel therapeutic strategies to combat this fatal disease.

Methods

Ethics statement

Human adult GBM tissue samples were obtained at the Neurosurgical Clinic of the University Hospital of Basel, Switzerland in accordance with the Swiss Human Research Act and institutional ethics commission (EKNZ 02019-02358). All patients gave written informed consent for tumor biopsy collection and signed a declaration permitting the use of their biopsy specimens in scientific research, including storage in our brain tumor biobank (Req-2019-00553). All patient identifying information was removed and tissue was coded for identification.

Glioma tissue dissociation

Resected glioma tissue samples were immediately placed on ice and transferred to the laboratory for single cell dissociation within 2-3 h after resection. Human brain tissue was manually minced using razor blades and enzymatically dissociated at 37°C for 30 minutes with 1 mg/ml collagenase-4 (#LS004188, Worthington Biochemical Corporation, USA) and 250 U/ml DNAse1 (#10104159001, Roche, Switzerland) in a buffer containing Hank's Balanced Salt Solution (HBSS) with Ca^{2+}/Mg^{2+}, 1% MEM non-essential amino acids (Gibco, USA), 1 mM sodium pyruvate (Gibco), 44 mM sodium bi-carbonate (Gibco), 25 mM HEPES (Gibco), 1% GlutaMAX (Gibco) and 1% antibiotic-antimycotic (Sigma-Aldrich, USA). Cells were filtered and separated from dead cells, debris and myelin by a 0.9 M sucrose (#84100, Simga Aldrich) density gradient centrifugation. Upon ACK-lysis for removal of erythrocytes (#A1049201, Gibco) the now generated single-cell suspension (SCS) was washed, counted and frozen in Bambanker (#BB01, Nippon Genetics, Germany) in liquid nitrogen until use.

PBMCs (Peripheral blood mononuclear cells) preparation

Patient blood samples were directly placed on ice and transferred to the laboratory for PBMC isolation. Blood samples were centrifuged to separate buffy coat from plasma and erythrocytes, followed by standard density gradient centrifugation protocol (#17144002, Ficoll-Paque PLUS, Cytiva, USA) to isolate PBMCs. PBMCs were frozen in Bambanker (#BB01, Nippon Genetics, Germany) in liquid nitrogen until use.

FACS sorting for single cell RNA sequencing (scRNA-seq)

Cryopreserved tumor digests from glioma samples (center and periphery), as well as autologous PBMCs were thawed and washed with excess ice-cold 1xPBS and spun down at

350xg for 5 min. Subsequently, the cells were stained with Live/Dead (APC-Cy7 (Near IR), # L34976, Thermo Fischer) and a cocktail of fluorescently-conjugated antibodies CD11b (FITC, clone M1/70, #101206, BioLegend) and CD45 (FITC, clone 2D1, #368508, BioLegend), and large debris were removed with a 40-µm strainer. All samples were acquired on the BD FACS ARIA Fusion III (Becton Dickinson GmbH, Germany). For single-cell RNA-seq experiments, live and single gated cells were sorted into non-immune cell ($CD45^{-}CD11b^{-}$) and immune cell ($CD45^{+}CD11b^{+}$) populations. Both populations were directly sorted into Eppendorf tubes with 1xPBS supplemented with 1% BSA for single cell RNA sequencing.

Single cell RNA sequencing (scRNA-seq) – Library preparation and sequencing

Single-cell RNA-seq was performed using Chromium Single Cell 3' GEM, Library & Gel Bead Kit v3 (#CG000183, 10x Genomics, Pleasanton, CA, USA) following the manufacturer's protocol. Briefly, non-immune cells and immune cells were mixed at a defined ratio of 1:4. Roughly 8000-10000 cells per sample, diluted at a density of 100–800 cells/µL in PBS plus 1% BSA determined by Cellometer Auto 2000 Cell Viability Counter (Nexelom Bioscience, Lawrence, MA USA), and were loaded onto the chip. The quality and concentration of both cDNA and libraries were assessed using an Agilent BioAnalyzer with High Sensitivity kit (#5067-4626, Agilent, Santa Clara, CA USA) and Qubit Fluorometer with dsDNA HS assay kit (#Q33230, Thermo Fischer Scientific, Waltham, MA USA) according to the manufacturer's recommendation. For sequencing, samples were mixed in equimolar fashion and sequenced on an Illumina HiSeq 4000 with a targeted read depth of 50,000 reads/cell and sequencing parameters were set for Read1 (28 cycles), Index1 (8 cycles), and Read2 (91 cycles).

Single cell RNA sequencing (scRNA-seq) - Computational analysis

The dataset was analyzed by the Bioinformatics Core Facility, Department of Biomedicine, University of Basel. Read quality was controlled with the FastQC tool (version 0.11.5). Sequencing files were processed using the Salmon Alevin tool (v 1.3.0) [71] to perform quality control, sample demultiplexing, cell barcode processing, pseudo-alignment of cDNA reads to the human Gencode v35 reference and counting of UMIs. Parameters *--keepCBFraction 1* and *--maxNumBarcodes 100000* were used.

Processing of the UMI counts matrix was performed using the Bioconductor packages DropletUtils (version 1.8.0) [72, 73], scran (version 1.16.0) [74, 75] and scater (version 1.16.2) [76], following mostly the steps illustrated in the OSCA book (http://bioconductor.org/books/release/OSCA/) [75, 77]. Filtering for high-quality cells was done based on

library size (at least 2,000 UMI counts per cell), the number of detected genes (at least 700 genes detected) and the percentage of reads mapping to mitochondrial genes (larger than 0% and lower than 15%), based on the distribution observed across cells. Low-abundance genes with average counts per cell lower than 0.006 were filtered out. The presence of doublet cells was investigated with the scDblFinder package (version 1.2.0), and suspicious cells were filtered out (score > 0.6). After quality filtering, the resulting dataset consisted of UMI counts for 15,523 genes and 45,466 cells, ranging from 803 to 9,121 per sample.

UMI counts were normalized with size factors estimated from pools of cells created with the scran package *quickCluster()* function [74, 78]. To distinguish between genuine biological variability and technical noise we modeled the variance of the log-expression across genes using a Poisson-based mean-variance trend. The scran package *denoisePCA()* function was used denoise log-expression data by removing principal components corresponding to technical noise. A t-stochastic neighbor embedding (t-SNE) was built with a perplexity of 50 using the top most variable genes (141 genes with estimated biological variance > 0.3, excluding genes with highest proportion of reads in the ambient RNA pool estimated from empty droplets), and the denoised principal components as input (5 top PCs). Clustering of cells was performed with hierarchical clustering on the Euclidean distances between cells (with Ward's criterion to minimize the total variance within each cluster [79]; package cluster version 2.1.0). The number of clusters used for following analyses was identified by applying a dynamic tree cut (package dynamicTreeCut, version 1.63-1) [80], resulting in 10, or 22 clusters with argument *deepSplit* set to 2.

The Bioconductor package SingleR (version 1.2.4) was used for cell-type annotation of the cells [81] using as references (i) a public bulk RNA-seq dataset of sorted immune cell types from human PBMC samples [13], available through the *celldex* Bioconductor package; (ii) a bulk RNA-seq dataset of sorted immune cell types from the tumor microenvironment of human gliomas [5] (UMI count matrix and annotation downloaded from https://joycelab.shinyapps.io/braintime/); (iii) a Smartseq2 scRNA-seq dataset of IDH-wild-type glioblastoma tumors [14] (downloaded from GEO accession GSE131928). A microglia and a macrophage signature scores were defined by averaging the center and scaled expression levels of gene lists obtained in [7]. An endothelial score was defined by averaging the center and scaled expression levels of the genes *CDH5*, *VWF*, *CD34* and *PECAM1*. The SingleR high-quality assignments (pruned scores) and the signature scores were used to manually derive a consensus cell type annotation for each cluster.

The *findMarkers* function of the scran package was used to find the best markers across annotated cell types (parameters *direction="up"* and *pval.type="any"*). The top 10 markers for each cell type were extracted and pooled to from a list of 68 markers.

Differential abundance analysis of identified cell types between tumor sites was performed using *diffcyt-DA-voom* method [82]. Differential abundance of cell types was considered to be significant at a false discovery rate (FDR) lower than 5 %.

Differential expression between tumor sites, or between PBMC cells and tumor periphery cells, stratified by annotated cell type, was performed using a pseudo-bulk approach, summing the UMI counts of cells from each cell type in each sample when at least 20 cells could be aggregated. The aggregated samples were then treated as bulk RNA-seq samples [83] and for each pairwise comparison genes were filtered to keep genes detected in at least 5% of the cells aggregated. The package edgeR (version 3.30.3) [84] was used to perform TMM normalization [85] and to test for differential expression with the Generalized Linear Model (GLM) framework, using a model accounting for patient-specific effects. Genes with a FDR lower than 5 % were considered differentially expressed. Gene set enrichment analysis was performed with the function camera [86] on gene sets from the Molecular Signature Database (MSigDB, version 7.4) [39, 87]. We retained only sets containing more than 5 genes, and gene sets with a FDR lower than 5% were considered as significant.

Cell chat analysis

The R package CellChat (1.1.3) [60] was used to analyze cell-cell interactions in our dataset (with previously annotated 9 cell types). We followed the recommended workflow to infer the cell state-specific communications (using *identifyOverExpressedGenes*, *identifyOverExpressedInteractions* and *projectData* with the default parameters). We performed 3 separate analyses, on the center and the periphery subsets and a comparison analysis as described in the official workflow. We visualized the significant interactions for the microglia cluster using *netVisual_chord_gene* and used *plotGeneExpression* to display of the expression of all genes involved SPP1 signaling pathway in the cell populations. Finally, *netAnalysis_signalingRole_scatter* was used to calculate and visualize incoming and outgoing signaling strength.

Flow cytometry analysis of paired PBMC and periphery samples

Cryopreserved samples were thawed and washed with excess ice-cold 1xPBS and spun down at 350xg for 5 min. Cells were resuspended in FACS buffer (PBS plus 2% FBS) and blocked with monoclonal antibody to CD16/32 (Human TruStain FcX, #422302, Biolegend)

for 10 min at 4°C before staining with surface antibodies: CD45RA (PE, clone HI100, #304108), CD45RO (APC, clone UCHL1, #304210), CD3e (BV650, clone UCHT1, #300468), CD8a (BV421, clone RPA-T8, #301036), CCR7 (FITC, clone G043H7, #353216), CD62L (AF700, clone DREG-56, #304820), CD69 (APC-Cy7, clone FN50, #310914), CD103 (PerCP/Cy5.5, clone Ber-ACT8, #350226) and CX3CR1 (PE/Cy7, clone 2A9-1, #341612). All antibodies were purchased from BioLegend, USA. Cells were stained for 30 min at 4°C, and subsequently washed with FACS buffer. To exclude dead cells Zombie Aqua Fixable Viability Kit (#423102, 1:100, BioLegend) was added. Acquisition was performed on a CytoFLEX (Beckman). Data was analyzed using FlowJo software, version 10.8.1 (TreeStar). Gates were drawn by using Fluorescent Minus One (FMO) controls.

Statistical analysis of flow cytometry data

Data analysis and graph generation was performed using GraphPad Prism 9 (GraphPad Prism Software Inc.). Paired comparisons between two groups were performed using Wilcoxon matched-pairs signed rank test. Differences of more than two paired groups were assessed using repeated measures one-way ANOVA test, followed by post-hoc Šidák's multiple comparisons correction. A p value < 0.05 was considered statistically significant. *$p \leq 0.05$, **$p \leq 0.01$, ***$p \leq 0.001$, ****$p \leq 0.0001$.

Data availability

The UMI count matrix and cell metadata from the scRNA-seq dataset are available on GEO under accession number GSE197543. The remaining data are available within the Article and Supplementary Information.

References

1. Stupp, R., W.P. Mason, M.J. van den Bent, M. Weller, B. Fisher, M.J. Taphoorn, K. Belanger, A.A. Brandes, C. Marosi, U. Bogdahn, J. Curschmann, R.C. Janzer, S.K. Ludwin, T. Gorlia, A. Allgeier, D. Lacombe, J.G. Cairncross, E. Eisenhauer, and R.O. Mirimanoff, *Radiotherapy plus concomitant and adjuvant temozolomide for glioblastoma.* N Engl J Med, 2005. **352**(10): p. 987-96.

2. Bowman, R.L., F. Klemm, L. Akkari, S.M. Pyonteck, L. Sevenich, D.F. Quail, S. Dhara, K. Simpson, E.E. Gardner, C.A. Iacobuzio-Donahue, C.W. Brennan, V. Tabar, P.H. Gutin, and J.A. Joyce, *Macrophage Ontogeny Underlies Differences in Tumor-Specific Education in Brain Malignancies.* Cell Rep, 2016. **17**(9): p. 2445-2459.

3. Reardon, D.A., T.J. Kaley, J. Dietrich, J.L. Clarke, G.P. Dunn, M. Lim, T.F. Cloughesy, H.K. Gan, A.J. Park, P. Schwarzenberger, T. Ricciardi, M.J. Macri, A. Ryan, and R.R. Venhaus, *Phase 2 study to evaluate safety and efficacy of MEDI4736 (durvalumab [DUR]) in glioblastoma (GBM) patients: An update.* Journal of Clinical Oncology, 2017. **35**(15_suppl): p. 2042-2042.

4. Reardon, D.A., A. Omuro, A.A. Brandes, J. Rieger, A. Wick, J. Sepulveda, S. Phuphanich, P. de Souza, M.S. Ahluwalia, M. Lim, G. Vlahovic, and J. Sampson, *OS10.3 Randomized Phase 3 Study Evaluating the Efficacy and Safety of Nivolumab vs Bevacizumab in Patients With Recurrent Glioblastoma: CheckMate 143.* Neuro-Oncology, 2017. **19**(Suppl 3): p. iii21-iii21.

5. Klemm, F., R.R. Maas, R.L. Bowman, M. Kornete, K. Soukup, S. Nassiri, J.P. Brouland, C.A. Iacobuzio-Donahue, C. Brennan, V. Tabar, P.H. Gutin, R.T. Daniel, M.E. Hegi, and J.A. Joyce, *Interrogation of the Microenvironmental Landscape in Brain Tumors Reveals Disease-Specific Alterations of Immune Cells.* Cell, 2020. **181**(7): p. 1643-1660.e17.

6. Friebel, E., K. Kapolou, S. Unger, N.G. Núñez, S. Utz, E.J. Rushing, L. Regli, M. Weller, M. Greter, S. Tugues, M.C. Neidert, and B. Becher, *Single-Cell Mapping of Human Brain Cancer Reveals Tumor-Specific Instruction of Tissue-Invading Leukocytes.* Cell, 2020. **181**(7): p. 1626-1642.e20.

7. Müller, S., G. Kohanbash, S.J. Liu, B. Alvarado, D. Carrera, A. Bhaduri, P.B. Watchmaker, G. Yagnik, E. Di Lullo, M. Malatesta, N.M. Amankulor, A.R. Kriegstein, D.A. Lim, M. Aghi, H. Okada, and A. Diaz, *Single-cell profiling of human gliomas reveals macrophage ontogeny as a basis for regional differences in macrophage activation in the tumor microenvironment.* Genome Biology, 2017. **18**(1): p. 234.

8. Abdelfattah, N., P. Kumar, C. Wang, J.-S. Leu, W.F. Flynn, R. Gao, D.S. Baskin, K. Pichumani, O.B. Ijare, S.L. Wood, S.Z. Powell, D.L. Haviland, B.C. Parker Kerrigan, F.F. Lang, S.S. Prabhu, K.M. Huntoon, W. Jiang, B.Y.S. Kim, J. George, and K. Yun, *Single-cell analysis of human glioma and immune cells identifies S100A4 as an immunotherapy target.* Nature Communications, 2022. **13**(1): p. 767.

9. Darmanis, S., S.A. Sloan, D. Croote, M. Mignardi, S. Chernikova, P. Samghababi, Y. Zhang, N. Neff, M. Kowarsky, C. Caneda, G. Li, S.D. Chang, I.D. Connolly, Y. Li, B.A. Barres, M.H. Gephart, and S.R. Quake, *Single-Cell RNA-Seq Analysis of Infiltrating Neoplastic Cells at the Migrating Front of Human Glioblastoma.* Cell Rep, 2017. **21**(5): p. 1399-1410.

10. Landry, A.P., M. Balas, S. Alli, J. Spears, and Z. Zador, *Distinct regional ontogeny and activation of tumor associated macrophages in human glioblastoma.* Scientific Reports, 2020. **10**(1): p. 19542.

11. Louis, D.N., A. Perry, P. Wesseling, D.J. Brat, I.A. Cree, D. Figarella-Branger, C. Hawkins, H.K. Ng, S.M. Pfister, G. Reifenberger, R. Soffietti, A. von Deimling, and D.W. Ellison, *The 2021 WHO Classification of Tumors of the Central Nervous System: a summary.* Neuro-Oncology, 2021. **23**(8): p. 1231-1251.

12. Linderman, G.C., M. Rachh, J.G. Hoskins, S. Steinerberger, and Y. Kluger, *Fast interpolation-based t-SNE for improved visualization of single-cell RNA-seq data.* Nat Methods, 2019. **16**(3): p. 243-245.

13. Monaco, G., B. Lee, W. Xu, S. Mustafah, Y.Y. Hwang, C. Carré, N. Burdin, L. Visan, M. Ceccarelli, M. Poidinger, A. Zippelius, J. Pedro de Magalhães, and A. Larbi, *RNA-Seq Signatures Normalized by mRNA Abundance Allow Absolute Deconvolution of Human Immune Cell Types.* Cell Rep, 2019. **26**(6): p. 1627-1640.e7.

14. Neftel, C., J. Laffy, M.G. Filbin, T. Hara, M.E. Shore, G.J. Rahme, A.R. Richman, D. Silverbush, M.L. Shaw, C.M. Hebert, J. Dewitt, S. Gritsch, E.M. Perez, L.N. Gonzalez Castro, X. Lan, N. Druck, C. Rodman, D. Dionne, A. Kaplan, M.S. Bertalan, J. Small, K. Pelton, S. Becker, D. Bonal, Q.-D. Nguyen, R.L. Servis, J.M. Fung, R. Mylvaganam, L. Mayr, J. Gojo, C. Haberler, R. Geyeregger, T. Czech, I. Slavc, B.V. Nahed, W.T. Curry, B.S. Carter, H. Wakimoto, P.K. Brastianos, T.T. Batchelor, A. Stemmer-Rachamimov, M. Martinez-Lage, M.P. Frosch, I. Stamenkovic, N. Riggi, E. Rheinbay, M. Monje, O. Rozenblatt-Rosen, D.P. Cahill, A.P. Patel, T. Hunter, I.M. Verma, K.L. Ligon, D.N. Louis, A. Regev, B.E. Bernstein, I. Tirosh, and M.L. Suvà, *An Integrative Model of Cellular States, Plasticity, and Genetics for Glioblastoma.* Cell, 2019. **178**(4): p. 835-849.e21.

15. Baek, M., E. Yoo, H.I. Choi, G.Y. An, J.C. Chai, Y.S. Lee, K.H. Jung, and Y.G. Chai, *The BET inhibitor attenuates the inflammatory response and cell migration in human microglial HMC3 cell line.* Scientific Reports, 2021. **11**(1): p. 8828.

16. Hagiwara, S., Y. Murakumo, S. Mii, T. Shigetomi, N. Yamamoto, H. Furue, M. Ueda, and M. Takahashi, *Processing of CD109 by furin and its role in the regulation of TGF-β signaling.* Oncogene, 2010. **29**(15): p. 2181-2191.

17. Traini, M., C.M. Quinn, C. Sandoval, E. Johansson, K. Schroder, M. Kockx, P.J. Meikle, W. Jessup, and L. Kritharides, *Sphingomyelin phosphodiesterase acid-like 3A (SMPDL3A) is a novel nucleotide phosphodiesterase regulated by cholesterol in human macrophages.* J Biol Chem, 2014. **289**(47): p. 32895-913.

18. Yamada, T., J. Komoto, T. Kasuya, Y. Takata, H. Ogawa, H. Mori, and F. Takusagawa, *A catalytic mechanism that explains a low catalytic activity of serine dehydratase like-1 from human cancer cells: crystal structure and site-directed mutagenesis studies.* Biochim Biophys Acta, 2008. **1780**(5): p. 809-18.

19. Pan, R.-Y., J. Ma, X.-X. Kong, X.-F. Wang, S.-S. Li, X.-L. Qi, Y.-H. Yan, J. Cheng, Q. Liu, W. Jin, C.-H. Tan, and Z. Yuan, *Sodium rutin ameliorates Alzheimer’s disease–like pathology by enhancing microglial amyloid-β clearance.* Science Advances, 2019. **5**(2): p. eaau6328.

20. Wang, G., L. Ding, C. Gao, N. Zhang, D. Gan, Y. Sun, L. Xu, Q. Luo, and Z. Jiang, *Neuroprotective effect of l-serine against white matter demyelination by harnessing and modulating inflammation in mice.* Neuropharmacology, 2019. **146**: p. 39-49.

21. Soroceanu, L., R. Murase, C. Limbad, E. Singer, J. Allison, I. Adrados, R. Kawamura, A. Pakdel, Y. Fukuyo, D. Nguyen, S. Khan, R. Arauz, G.L. Yount, D.H. Moore, P.Y. Desprez, and S.D. McAllister, *Id-1 is a key transcriptional regulator of glioblastoma aggressiveness and a novel therapeutic target.* Cancer Res, 2013. **73**(5): p. 1559-69.

22. Papaspyridonos, M., I. Matei, Y. Huang, M. do Rosario Andre, H. Brazier-Mitouart, J.C. Waite, A.S. Chan, J. Kalter, I. Ramos, Q. Wu, C. Williams, J.D. Wolchok, P.B. Chapman, H. Peinado, N. Anandasabapathy, A.J. Ocean, R.N. Kaplan, J.P. Greenfield, J. Bromberg, D. Skokos, and D. Lyden, *Id1 suppresses anti-tumour immune responses and promotes tumour progression by impairing myeloid cell maturation.* Nature Communications, 2015. **6**(1): p. 6840.

23. Grandemange, S., I. Aksentijevich, I. Jeru, A. Gul, and I. Touitou, *The regulation of MEFV expression and its role in health and familial Mediterranean fever.* Genes & Immunity, 2011. **12**(7): p. 497-503.

24. Sharma, S., S.K. Patnaik, R. Thomas Taggart, E.D. Kannisto, S.M. Enriquez, P. Gollnick, and B.E. Baysal, *APOBEC3A cytidine deaminase induces RNA editing in monocytes and macrophages.* Nature Communications, 2015. **6**(1): p. 6881.

25. Vicente, R., A. Escalada, M. Coma, G. Fuster, E. Sánchez-Tilló, C. López-Iglesias, C. Soler, C. Solsona, A. Celada, and A. Felipe, *Differential voltage-dependent K+ channel responses during proliferation and activation in macrophages.* J Biol Chem, 2003. **278**(47): p. 46307-20.

26. Chen, P., H. Zuo, H. Xiong, M.J. Kolar, Q. Chu, A. Saghatelian, D.J. Siegwart, and Y. Wan, *Gpr132 sensing of lactate mediates tumor-macrophage interplay to promote breast cancer metastasis.* Proc Natl Acad Sci U S A, 2017. **114**(3): p. 580-585.

27. Gao, L., D.D. Xiong, R.Q. He, X. Yang, Z.F. Lai, L.M. Liu, Z.G. Huang, H.Y. Wu, L.H. Yang, J. Ma, S.H. Li, P. Lin, H. Yang, D.Z. Luo, Y.W. Dang, and G. Chen, *MIR22HG As A Tumor Suppressive lncRNA In HCC: A Comprehensive Analysis Integrating RT-qPCR, mRNA-Seq, And Microarrays.* Onco Targets Ther, 2019. **12**: p. 9827-9848.

28. Xiong, D., Y. Wang, and M. You, *A gene expression signature of TREM2hi macrophages and γδ T cells predicts immunotherapy response.* Nature Communications, 2020. **11**(1): p. 5084.

29. Vuletic, S., W. Dong, G. Wolfbauer, C. Tang, and J.J. Albers, *PLTP regulates STAT3 and NFκB in differentiated THP1 cells and human monocyte-derived macrophages.* Biochimica et Biophysica Acta (BBA) - Molecular Cell Research, 2011. **1813**(10): p. 1917-1924.

30. Casazza, A., D. Laoui, M. Wenes, S. Rizzolio, N. Bassani, M. Mambretti, S. Deschoemaeker, Jo A. Van Ginderachter, L. Tamagnone, and M. Mazzone, *Impeding Macrophage Entry into Hypoxic Tumor Areas by Sema3A/Nrp1 Signaling Blockade Inhibits Angiogenesis and Restores Antitumor Immunity.* Cancer Cell, 2013. **24**(6): p. 695-709.

31. Sadik, A., L.F. Somarribas Patterson, S. Öztürk, S.R. Mohapatra, V. Panitz, P.F. Secker, P. Pfänder, S. Loth, H. Salem, M.T. Prentzell, B. Berdel, M. Iskar, E. Faessler, F. Reuter, I. Kirst, V. Kalter, K.I. Foerster, E. Jäger, C.R. Guevara, M. Sobeh, T. Hielscher, G. Poschet, A. Reinhardt, J.C. Hassel, M. Zapatka, U. Hahn, A. von Deimling, C. Hopf, R. Schlichting, B.I. Escher, J. Burhenne, W.E. Haefeli, N. Ishaque, A. Böhme, S. Schäuble, K. Thedieck, S. Trump, M. Seiffert, and C.A. Opitz, *IL4I1 Is a Metabolic Immune Checkpoint that Activates the AHR and Promotes Tumor Progression.* Cell, 2020. **182**(5): p. 1252-1270.e34.

32. Rodriguez, A.E., G.S. Ducker, L.K. Billingham, C.A. Martinez, N. Mainolfi, V. Suri, A. Friedman, M.G. Manfredi, S.E. Weinberg, J.D. Rabinowitz, and N.S. Chandel, *Serine Metabolism Supports Macrophage IL-1β Production.* Cell Metabolism, 2019. **29**(4): p. 1003-1011.e4.

33. Tseng, W.C., V. Reinhart, T.A. Lanz, M.L. Weber, J. Pang, K.X.V. Le, R.D. Bell, P. O'Donnell, and D.L. Buhl, *Schizophrenia-associated SLC39A8 polymorphism is a loss-of-function allele altering glutamate receptor and innate immune signaling.* Translational Psychiatry, 2021. **11**(1): p. 136.

34. Holtman, I.R., D. Skola, and C.K. Glass, *Transcriptional control of microglia phenotypes in health and disease.* The Journal of Clinical Investigation, 2017. **127**(9): p. 3220-3229.

35. Nomaru, H., K. Sakumi, A. Katogi, Y.N. Ohnishi, K. Kajitani, D. Tsuchimoto, E.J. Nestler, and Y. Nakabeppu, *Fosb gene products contribute to excitotoxic microglial activation by regulating the expression of complement C5a receptors in microglia.* Glia, 2014. **62**(8): p. 1284-98.

36. Sweet, D.R., N.T. Vasudevan, L. Fan, C.E. Booth, K.S. Keerthy, X. Liao, V. Vinayachandran, Y. Takami, D. Tugal, N. Sharma, E.R. Chan, L. Zhang, Y. Qing, S.L. Gerson, C. Fu, A. Wynshaw-Boris, P. Sangwung, L. Nayak, P. Holvoet, K. Matoba, Y. Lu, G. Zhou, and M.K. Jain, *Myeloid Krüppel-like factor 2 is a critical regulator of metabolic inflammation.* Nature Communications, 2020. **11**(1): p. 5872.

37. Salojin, K.V., I.B. Owusu, K.A. Millerchip, M. Potter, K.A. Platt, and T. Oravecz, *Essential role of MAPK phosphatase-1 in the negative control of innate immune responses.* J Immunol, 2006. **176**(3): p. 1899-907.

38. Lee, H., S. Cha, M.S. Lee, G.J. Cho, W.S. Choi, and K. Suk, *Role of antiproliferative B cell translocation gene-1 as an apoptotic sensitizer in activation-induced cell death of brain microglia.* J Immunol, 2003. **171**(11): p. 5802-11.

39. Liberzon, A., C. Birger, H. Thorvaldsdóttir, M. Ghandi, J.P. Mesirov, and P. Tamayo, *The Molecular Signatures Database (MSigDB) hallmark gene set collection.* Cell systems, 2015. **1**(6): p. 417-425.

40. Walker, D.G. and L.F. Lue, *Immune phenotypes of microglia in human neurodegenerative disease: challenges to detecting microglial polarization in human brains.* Alzheimers Res Ther, 2015. **7**(1): p. 56.

41. Hopperton, K.E., D. Mohammad, M.O. Trépanier, V. Giuliano, and R.P. Bazinet, *Markers of microglia in post-mortem brain samples from patients with Alzheimer's disease: a systematic review.* Molecular Psychiatry, 2018. **23**(2): p. 177-198.

42. Hammond, T.R., C. Dufort, L. Dissing-Olesen, S. Giera, A. Young, A. Wysoker, A.J. Walker, F. Gergits, M. Segel, J. Nemesh, S.E. Marsh, A. Saunders, E. Macosko, F. Ginhoux, J. Chen, R.J.M. Franklin, X. Piao, S.A. McCarroll, and B. Stevens, *Single-Cell RNA Sequencing of Microglia throughout the Mouse Lifespan and in the Injured Brain Reveals Complex Cell-State Changes.* Immunity, 2019. **50**(1): p. 253-271.e6.

43. McQuade, A., Y.J. Kang, J. Hasselmann, A. Jairaman, A. Sotelo, M. Coburn, S.K. Shabestari, J.P. Chadarevian, G. Fote, C.H. Tu, E. Danhash, J. Silva, E. Martinez, C. Cotman, G.A. Prieto, L.M. Thompson, J.S. Steffan, I. Smith, H. Davtyan, M. Cahalan, H. Cho, and M. Blurton-Jones, *Gene expression and functional deficits underlie TREM2-knockout microglia responses in human models of Alzheimer's disease.* Nature Communications, 2020. **11**(1): p. 5370.

44. Saijo, K., B. Winner, C.T. Carson, J.G. Collier, L. Boyer, M.G. Rosenfeld, F.H. Gage, and C.K. Glass, *A Nurr1/CoREST pathway in microglia and astrocytes protects dopaminergic neurons from inflammation-induced death.* Cell, 2009. **137**(1): p. 47-59.

45. Rothe, T., N. Ipseiz, M. Faas, S. Lang, F. Perez-Branguli, D. Metzger, H. Ichinose, B. Winner, G. Schett, and G. Krönke, *The Nuclear Receptor Nr4a1 Acts as a Microglia Rheostat and Serves as a Therapeutic Target in Autoimmune-Driven Central Nervous System Inflammation.* Journal of immunology (Baltimore, Md. : 1950), 2017. **198**(10): p. 3878-3885.

46. Szabo, P.A., H.M. Levitin, M. Miron, M.E. Snyder, T. Senda, J. Yuan, Y.L. Cheng, E.C. Bush, P. Dogra, P. Thapa, D.L. Farber, and P.A. Sims, *Single-cell transcriptomics of human T cells reveals tissue and activation signatures in health and disease.* Nature Communications, 2019. **10**(1): p. 4706.

47. Alegre, M.L., P.J. Noel, B.J. Eisfelder, E. Chuang, M.R. Clark, S.L. Reiner, and C.B. Thompson, *Regulation of surface and intracellular expression of CTLA4 on mouse T cells.* J Immunol, 1996. **157**(11): p. 4762-70.

48. Johnson, D.B., M.J. Nixon, Y. Wang, D.Y. Wang, E. Castellanos, M.V. Estrada, P.I. Ericsson-Gonzalez, C.H. Cote, R. Salgado, V. Sanchez, P.T. Dean, S.R. Opalenik, D.M. Schreeder, D.L. Rimm, J.Y. Kim, J. Bordeaux, S. Loi, L. Horn, M.E. Sanders, P.B. Ferrell, Jr., Y. Xu, J.A. Sosman, R.S. Davis, and J.M. Balko, *Tumor-specific MHC-II expression drives a unique pattern of resistance to immunotherapy via LAG-3/FCRL6 engagement.* JCI insight, 2018. **3**(24): p. e120360.

49. Sciumè, G., G. De Angelis, G. Benigni, A. Ponzetta, S. Morrone, A. Santoni, and G. Bernardini, *CX3CR1 expression defines 2 KLRG1+ mouse NK-cell subsets with distinct functional properties and positioning in the bone marrow.* Blood, 2011. **117**(17): p. 4467-4475.

50. Böttcher, J.P., M. Beyer, F. Meissner, Z. Abdullah, J. Sander, B. Höchst, S. Eickhoff, J.C. Rieckmann, C. Russo, T. Bauer, T. Flecken, D. Giesen, D. Engel, S. Jung, D.H. Busch, U. Protzer, R. Thimme, M. Mann, C. Kurts, J.L. Schultze, W. Kastenmüller, and P.A. Knolle, *Functional classification of memory CD8+ T cells by CX3CR1 expression.* Nature Communications, 2015. **6**(1): p. 8306.

51. Gerlach, C., E.A. Moseman, S.M. Loughhead, D. Alvarez, A.J. Zwijnenburg, L. Waanders, R. Garg, J.C. de la Torre, and U.H. von Andrian, *The Chemokine Receptor*

CX3CR1 Defines Three Antigen-Experienced CD8 T Cell Subsets with Distinct Roles in Immune Surveillance and Homeostasis. Immunity, 2016. **45**(6): p. 1270-1284.

52. Urban, S.L., I.J. Jensen, Q. Shan, L.L. Pewe, H.-H. Xue, V.P. Badovinac, and J.T. Harty, *Peripherally induced brain tissue–resident memory CD8+ T cells mediate protection against CNS infection.* Nature Immunology, 2020. **21**(8): p. 938-949.

53. Mackay, L.K., M. Minnich, N.A. Kragten, Y. Liao, B. Nota, C. Seillet, A. Zaid, K. Man, S. Preston, D. Freestone, A. Braun, E. Wynne-Jones, F.M. Behr, R. Stark, D.G. Pellicci, D.I. Godfrey, G.T. Belz, M. Pellegrini, T. Gebhardt, M. Busslinger, W. Shi, F.R. Carbone, R.A. van Lier, A. Kallies, and K.P. van Gisbergen, *Hobit and Blimp1 instruct a universal transcriptional program of tissue residency in lymphocytes.* Science, 2016. **352**(6284): p. 459-63.

54. Ma, J., B. Zheng, S. Goswami, L. Meng, D. Zhang, C. Cao, T. Li, F. Zhu, L. Ma, Z. Zhang, S. Zhang, M. Duan, Q. Chen, Q. Gao, and X. Zhang, *PD1(Hi) CD8(+) T cells correlate with exhausted signature and poor clinical outcome in hepatocellular carcinoma.* Journal for immunotherapy of cancer, 2019. **7**(1): p. 331-331.

55. Liu, X., Y. Wang, H. Lu, J. Li, X. Yan, M. Xiao, J. Hao, A. Alekseev, H. Khong, T. Chen, R. Huang, J. Wu, Q. Zhao, Q. Wu, S. Xu, X. Wang, W. Jin, S. Yu, Y. Wang, L. Wei, A. Wang, B. Zhong, L. Ni, X. Liu, R. Nurieva, L. Ye, Q. Tian, X.-W. Bian, and C. Dong, *Genome-wide analysis identifies NR4A1 as a key mediator of T cell dysfunction.* Nature, 2019. **567**(7749): p. 525-529.

56. Dan, L., L. Liu, Y. Sun, J. Song, Q. Yin, G. Zhang, F. Qi, Z. Hu, Z. Yang, Z. Zhou, Y. Hu, L. Zhang, J. Ji, X. Zhao, Y. Jin, M.A. McNutt, and Y. Yin, *The phosphatase PAC1 acts as a T cell suppressor and attenuates host antitumor immunity.* Nature Immunology, 2020. **21**(3): p. 287-297.

57. Bignon, A., A. Régent, L. Klipfel, A. Desnoyer, P. de la Grange, V. Martinez, O. Lortholary, A. Dalloul, L. Mouthon, and K. Balabanian, *DUSP4-mediated accelerated T-cell senescence in idiopathic CD4 lymphopenia.* Blood, 2015. **125**(16): p. 2507-18.

58. Maine, C.J., J.R. Teijaro, K. Marquardt, and L.A. Sherman, *PTPN22 contributes to exhaustion of T lymphocytes during chronic viral infection.* Proceedings of the National Academy of Sciences, 2016. **113**(46): p. E7231-E7239.

59. Li, H., A.M. van der Leun, I. Yofe, Y. Lubling, D. Gelbard-Solodkin, A.C.J. van Akkooi, M. van den Braber, E.A. Rozeman, J.B.A.G. Haanen, C.U. Blank, H.M. Horlings, E. David, Y. Baran, A. Bercovich, A. Lifshitz, T.N. Schumacher, A. Tanay, and I. Amit, *Dysfunctional CD8 T Cells Form a Proliferative, Dynamically Regulated Compartment within Human Melanoma.* Cell, 2019. **176**(4): p. 775-789.e18.

60. Jin, S., C.F. Guerrero-Juarez, L. Zhang, I. Chang, R. Ramos, C.-H. Kuan, P. Myung, M.V. Plikus, and Q. Nie, *Inference and analysis of cell-cell communication using CellChat.* Nature Communications, 2021. **12**(1): p. 1088.

61. Wei, J., A. Marisetty, B. Schrand, K. Gabrusiewicz, Y. Hashimoto, M. Ott, Z. Grami, L.Y. Kong, X. Ling, H. Caruso, S. Zhou, Y.A. Wang, G.N. Fuller, J. Huse, E. Gilboa, N. Kang, X. Huang, R. Verhaak, S. Li, and A.B. Heimberger, *Osteopontin mediates glioblastoma-associated macrophage infiltration and is a potential therapeutic target.* J Clin Invest, 2019. **129**(1): p. 137-149.

915 62. Gandoglia, I., F. Ivaldi, P. Carrega, E. Armentani, G. Ferlazzo, G. Mancardi, N. Kerlero
916 de Rosbo, A. Uccelli, and A. Laroni, *In vitro VLA-4 blockade results in an impaired NK*
917 *cell-mediated immune surveillance against melanoma.* Immunology Letters, 2017. **181**:
918 p. 109-115.

919 63. Klement, J.D., A.V. Paschall, P.S. Redd, M.L. Ibrahim, C. Lu, D. Yang, E. Celis, S.I.
920 Abrams, K. Ozato, and K. Liu, *An osteopontin/CD44 immune checkpoint controls*
921 *CD8+ T cell activation and tumor immune evasion.* J Clin Invest, 2018. **128**(12): p.
922 5549-5560.

923 64. Olah, M., V. Menon, N. Habib, M.F. Taga, Y. Ma, C.J. Yung, M. Cimpean, A.
924 Khairallah, G. Coronas-Samano, R. Sankowski, D. Grün, A.A. Kroshilina, D. Dionne,
925 R.A. Sarkis, G.R. Cosgrove, J. Helgager, J.A. Golden, P.B. Pennell, M. Prinz, J.P.G.
926 Vonsattel, A.F. Teich, J.A. Schneider, D.A. Bennett, A. Regev, W. Elyaman, E.M.
927 Bradshaw, and P.L. De Jager, *Single cell RNA sequencing of human microglia uncovers*
928 *a subset associated with Alzheimer's disease.* Nature Communications, 2020. **11**(1): p.
929 6129.

930 65. Yan, Y., S. Cao, X. Liu, S.M. Harrington, W.E. Bindeman, A.A. Adjei, J.S. Jang, J. Jen,
931 Y. Li, P. Chanana, A.S. Mansfield, S.S. Park, S.N. Markovic, R.S. Dronca, and H.
932 Dong, *CX3CR1 identifies PD-1 therapy-responsive CD8+ T cells that withstand*
933 *chemotherapy during cancer chemoimmunotherapy.* JCI Insight, 2018. **3**(8).

934 66. Yamauchi, T., T. Hoki, T. Oba, V. Jain, H. Chen, K. Attwood, S. Battaglia, S. George,
935 G. Chatta, I. Puzanov, C. Morrison, K. Odunsi, B.H. Segal, G.K. Dy, M.S. Ernstoff, and
936 F. Ito, *T-cell CX3CR1 expression as a dynamic blood-based biomarker of response to*
937 *immune checkpoint inhibitors.* Nature Communications, 2021. **12**(1): p. 1402.

938 67. Smolders, J., K.M. Heutinck, N.L. Fransen, E.B.M. Remmerswaal, P. Hombrink, I.J.M.
939 ten Berge, R.A.W. van Lier, I. Huitinga, and J. Hamann, *Tissue-resident memory T cells*
940 *populate the human brain.* Nature Communications, 2018. **9**(1): p. 4593.

941 68. Kumar, B.V., W. Ma, M. Miron, T. Granot, R.S. Guyer, D.J. Carpenter, T. Senda, X.
942 Sun, S.H. Ho, H. Lerner, A.L. Friedman, Y. Shen, and D.L. Farber, *Human Tissue-*
943 *Resident Memory T Cells Are Defined by Core Transcriptional and Functional*
944 *Signatures in Lymphoid and Mucosal Sites.* Cell Rep, 2017. **20**(12): p. 2921-2934.

945 69. Mackay, L.K., A. Rahimpour, J.Z. Ma, N. Collins, A.T. Stock, M.L. Hafon, J. Vega-
946 Ramos, P. Lauzurica, S.N. Mueller, T. Stefanovic, D.C. Tscharke, W.R. Heath, M.
947 Inouye, F.R. Carbone, and T. Gebhardt, *The developmental pathway for*
948 *CD103(+)CD8+ tissue-resident memory T cells of skin.* Nat Immunol, 2013. **14**(12): p.
949 1294-301.

950 70. Mathewson, N.D., O. Ashenberg, I. Tirosh, S. Gritsch, E.M. Perez, S. Marx, L. Jerby-
951 Arnon, R. Chanoch-Myers, T. Hara, A.R. Richman, Y. Ito, J. Pyrdol, M. Friedrich, K.
952 Schumann, M.J. Poitras, P.C. Gokhale, L.N. Gonzalez Castro, M.E. Shore, C.M.
953 Hebert, B. Shaw, H.L. Cahill, M. Drummond, W. Zhang, O. Olawoyin, H. Wakimoto,
954 O. Rozenblatt-Rosen, P.K. Brastianos, X.S. Liu, P.S. Jones, D.P. Cahill, M.P. Frosch,
955 D.N. Louis, G.J. Freeman, K.L. Ligon, A. Marson, E.A. Chiocca, D.A. Reardon, A.
956 Regev, M.L. Suvà, and K.W. Wucherpfennig, *Inhibitory CD161 receptor identified in*
957 *glioma-infiltrating T cells by single-cell analysis.* Cell, 2021. **184**(5): p. 1281-1298.e26.

71. Srivastava, A., L. Malik, T. Smith, I. Sudbery, and R. Patro, *Alevin efficiently estimates accurate gene abundances from dscRNA-seq data.* Genome Biol, 2019. **20**(1): p. 65.

72. Griffiths, J.A., A.C. Richard, K. Bach, A.T.L. Lun, and J.C. Marioni, *Detection and removal of barcode swapping in single-cell RNA-seq data.* Nat Commun, 2018. **9**(1): p. 2667.

73. Lun, A.T.L., S. Riesenfeld, T. Andrews, T.P. Dao, T. Gomes, J. participants in the 1st Human Cell Atlas, and J.C. Marioni, *EmptyDrops: distinguishing cells from empty droplets in droplet-based single-cell RNA sequencing data.* Genome Biol, 2019. **20**(1): p. 63.

74. Vallejos, C.A., D. Risso, A. Scialdone, S. Dudoit, and J.C. Marioni, *Normalizing single-cell RNA sequencing data: challenges and opportunities.* Nat Meth, 2017. **14**(6): p. 565-571.

75. Lun, A., D. McCarthy, and J. Marioni, *A step-by-step workflow for low-level analysis of single-cell RNA-seq data with Bioconductor [version 2; referees: 3 approved, 2 approved with reservations].* F1000Research, 2016. **5**(2122).

76. McCarthy, D.J., K.R. Campbell, Q.F. Wills, and A.T.L. Lun, *Scater: pre-processing, quality control, normalization and visualization of single-cell RNA-seq data in R.* Bioinformatics, 2017. **33**(8): p. 1179-1186.

77. Amezquita, R.A., A.T.L. Lun, E. Becht, V.J. Carey, L.N. Carpp, L. Geistlinger, F. Martini, K. Rue-Albrecht, D. Risso, C. Soneson, L. Waldron, H. Pages, M.L. Smith, W. Huber, M. Morgan, R. Gottardo, and S.C. Hicks, *Orchestrating single-cell analysis with Bioconductor.* Nat Methods, 2019.

78. Lun, A.T., D.J. McCarthy, and J.C. Marioni, *A step-by-step workflow for low-level analysis of single-cell RNA-seq data with Bioconductor.* F1000Res, 2016. **5**: p. 2122.

79. Murtagh, F. and P. Legendre, *Ward's Hierarchical Agglomerative Clustering Method: Which Algorithms Implement Ward's Criterion?* J. Classif., 2014. **31**(3): p. 274–295.

80. Langfelder, P., B. Zhang, and S. Horvath, *Defining clusters from a hierarchical cluster tree: the Dynamic Tree Cut package for R.* Bioinformatics, 2008. **24**(5): p. 719-20.

81. Aran, D., A.P. Looney, L. Liu, E. Wu, V. Fong, A. Hsu, S. Chak, R.P. Naikawadi, P.J. Wolters, A.R. Abate, A.J. Butte, and M. Bhattacharya, *Reference-based analysis of lung single-cell sequencing reveals a transitional profibrotic macrophage.* Nat Immunol, 2019. **20**(2): p. 163-172.

82. Weber, L.M., M. Nowicka, C. Soneson, and M.D. Robinson, *diffcyt: Differential discovery in high-dimensional cytometry via high-resolution clustering.* Communications Biology, 2019. **2**(1): p. 183.

83. Lun, A.T.L. and J.C. Marioni, *Overcoming confounding plate effects in differential expression analyses of single-cell RNA-seq data.* Biostatistics, 2017. **18**(3): p. 451-464.

84. Robinson, M.D., D.J. McCarthy, and G.K. Smyth, *edgeR: a Bioconductor package for differential expression analysis of digital gene expression data.* Bioinformatics, 2010. **26**(1): p. 139-140.

998 85. Robinson, M.D. and A. Oshlack, *A scaling normalization method for differential*
999 *expression analysis of RNA-seq data.* Genome Biol, 2010. **11**(3): p. R25.

1000 86. Wu, D. and G.K. Smyth, *Camera: a competitive gene set test accounting for inter-gene*
1001 *correlation.* Nucleic Acids Res, 2012. **40**(17): p. e133.

1002 87. Subramanian, A., P. Tamayo, V.K. Mootha, S. Mukherjee, B.L. Ebert, M.A. Gillette,
1003 A. Paulovich, S.L. Pomeroy, T.R. Golub, E.S. Lander, and J.P. Mesirov, *Gene set*
1004 *enrichment analysis: A knowledge-based approach for interpreting genome-wide*
1005 *expression profiles.* Proc Natl Acad Sci U S A, 2005. **102**(43): p. 15545-15550.

1006

Acknowledgements

We are grateful to the patients and their families for their consent to donate tissue to our brain tumor biobank. We thank Tamara Hüssen, Alison Riberio and Florian Limani for experimental support and Cecile Buenter for critical revision of the manuscript. Calculations were performed at sciCORE (http://scicore.unibas.ch/) scientific computing center at the University of Basel. This work was supported by a Swiss Cancer Research MD-PhD Grant (MD-PhD-4818-06-2019) to P.S. as well an Alumni Medizin Basel grant to P.S.; Swiss National Science Foundation Professorial Fellowship (PP00P3_176974); the ProPatient Forschungsstiftung, University Hospital Basel (Annemarie Karrasch Award 2019); Swiss Cancer Research Grant (KFS- 4382-02-2018) to G.H.; the Department of Surgery, University Hospital Basel, to G.H. and P.S.; and by The Brain Tumour Charity Foundation, London, UK (GN- 000562) to G.H.

Author contribution

G.H., S. Herter, M.B., S.D. and P.S., conceived and planned the project. J.R. and S. Hogan analyzed the scRNA-sequencing data and performed statistical analysis. P.S. and S.D., performed experiments and interpreted the results. T.S., T.A.M. and M.-F.R. helped coordinating experiments. P.S. wrote the manuscript. G.H. supervised and coordinated the study and critically revised the manuscript. All authors reviewed the paper and approved its final version.

Competing interests

G.H. has equity in, and is a cofounder of Incephalo Inc.

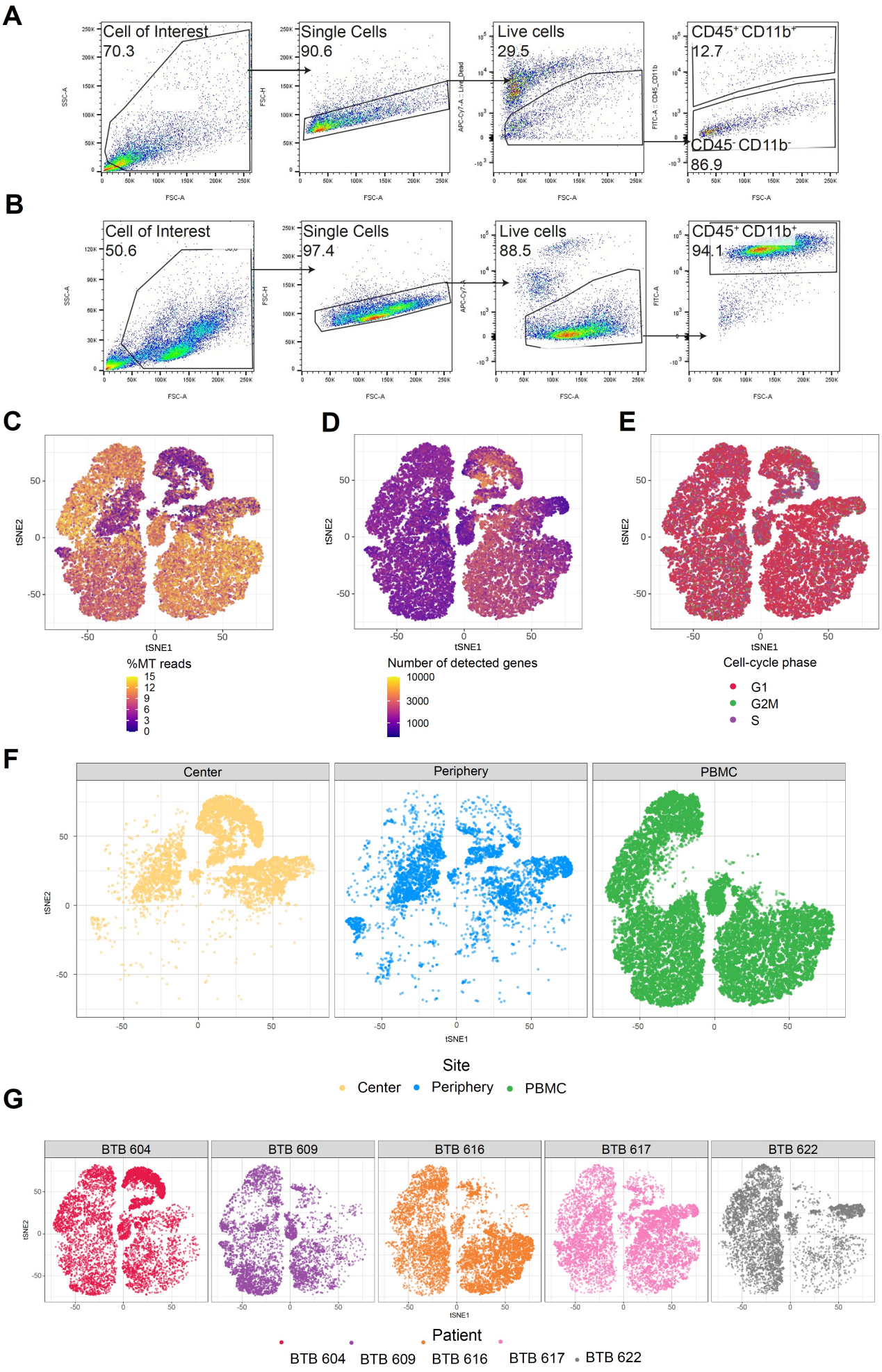
A
Cell of Interest
70.3
Single Cells
90.6
Live cells
29.5
CD45+ CD11b+
12.7
CD45- CD11b-
86.9
B
Cell of Interest
50.6
Single Cells
97.4
Live cells
88.5
CD45+ CD11b+
94.1
C
%MT reads
15
12
9
6
3
0
D
Number of detected genes
10000
3000
1000
E
Cell-cycle phase
G1
G2M
S
F
Center
Periphery
PBMC
Site
Center
Periphery
PBMC
G
BTB 604
BTB 609
BTB 616
BTB 617
BTB 622
Patient
BTB 604
BTB 609
BTB 616
BTB 617
BTB 622
tSNE1
tSNE2

Figure S1. $CD45^+$ $CD11b^+$ immune cells gating strategy and quality control of scRNA-seq data, related to Figures 1 and 2.

(A and B) Gating strategy for paired tumor-derived (A) and PBMCs (B); after debris, doublet and dead cell removal, immune cells were assessed as $CD45^+$ and/or $CD11b^+$.

(C-E) Percentage of mitochondrial (MT) reads (C) number of detected genes (D) and cell-cycle phase (E) overlaid on tSNE representation.

(F and G) tSNE map stratified according to site (F) and patient (G).

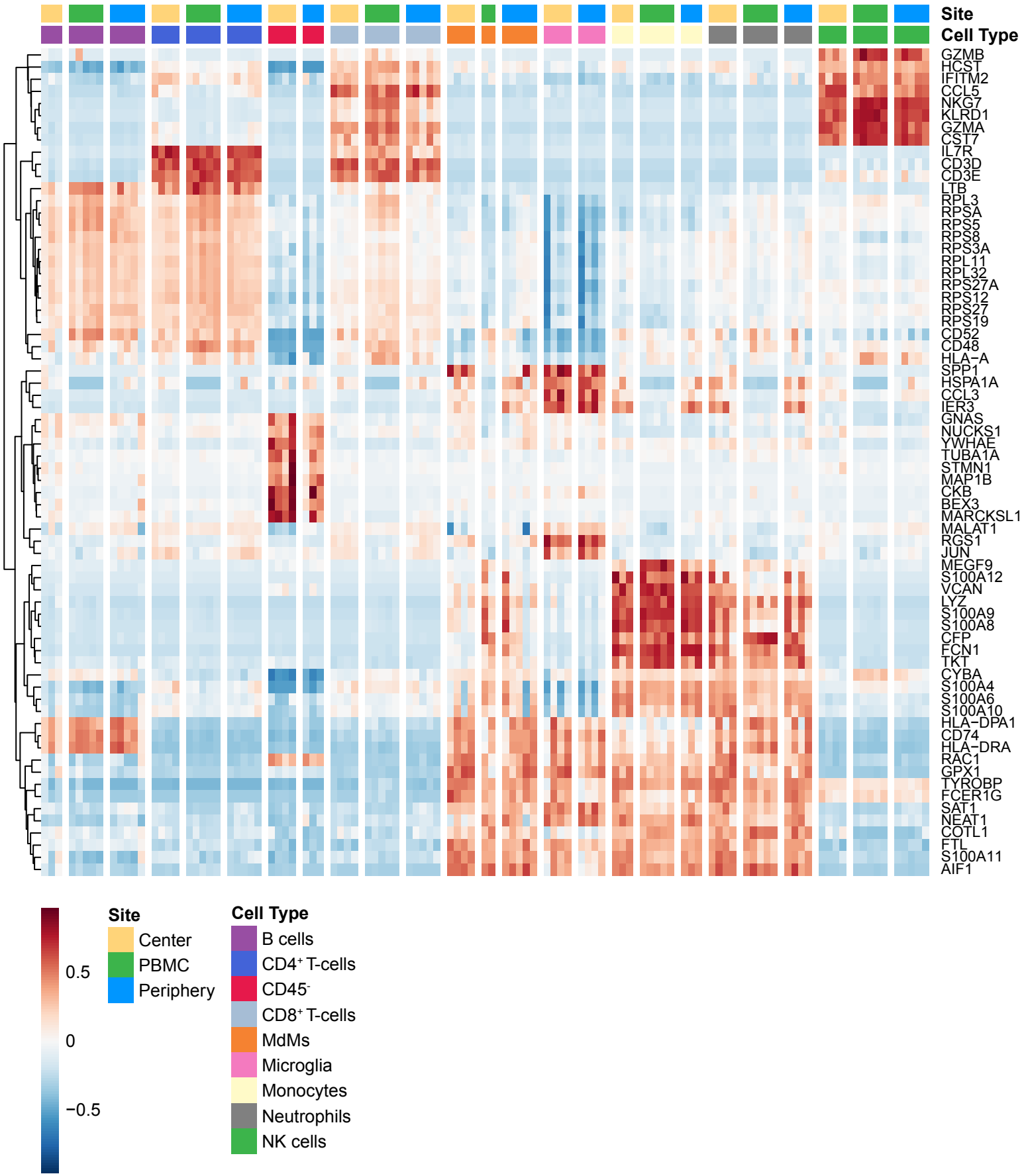

Figure S2. Cell type specific gene expression, related to Figure 2.

Heatmap displaying genes whose expression is most specific to each cell type. Columns are ordered by site and cell type, and rows show centered and scaled expression values, hierarchically clustered.

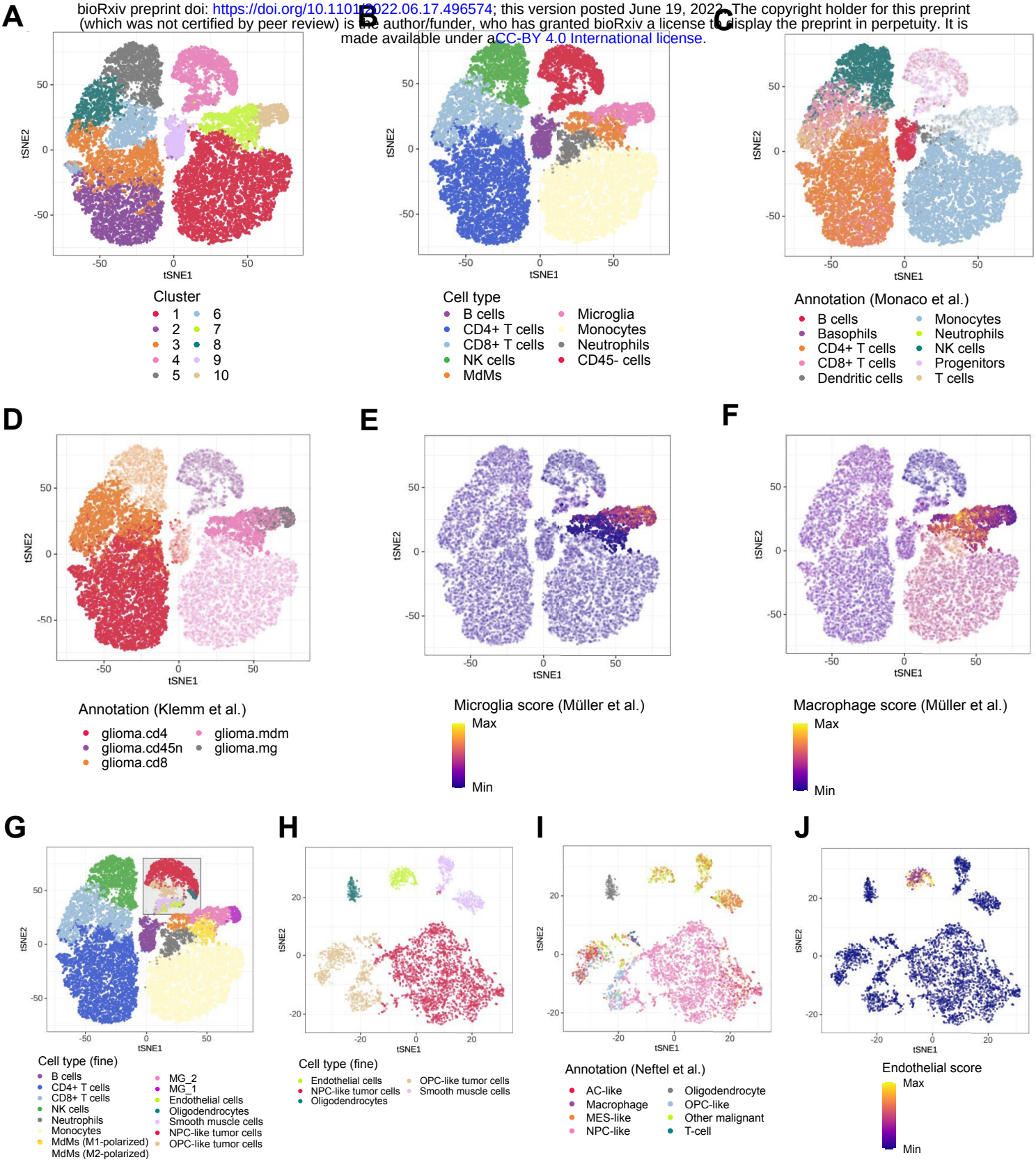

Figure S3. Cross-referencing scRNA-seq data with published datasets, related to Figure 2.

(A, B, G and H) Using hierarchical clustering, identified cell clusters (A) which were then annotated into eight distinct cell types for the immune subset (B) and five cell types for the $CD45^{neg}$ subset (G and H). Grey panel in (G) zooms in on $CD45^{neg}$ subset and is shown in (H).

(C-F) Immune cell types were annotated by referencing to a dataset of bulk RNA-seq samples of sorted immune cell types from human PBMC (C) [1]; MdMs and microglia were annotated by comparing to a dataset of bulk RNA-seq samples of sorted immune cell types from the tumor microenvironment of human gliomas (D) [2] and by using signature scores defined from scRNA-seq of glioma TAMs (E and F) [3]. Clusters are highlighted which were annotated using each respective reference dataset.

(I) $CD45^{neg}$ cells were annotated by whole-transcriptome comparison to a scRNA-seq dataset of IDH1wt GBM [4].

(J) Endothelial score was defined by averaging the center and scaled expression levels of the genes CDH5, VWF, CD34 and PECAM1.

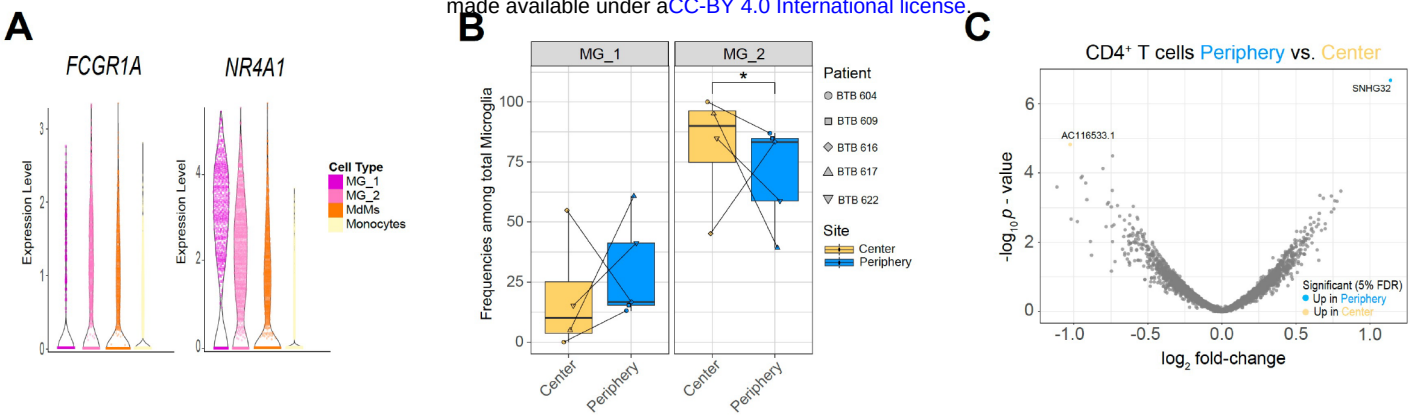

Figure S4. Differential abundance of MG subclusters and differential expression between center and peripheral CD4$^+$ T cells, related to Figures 3 and 4.

(A) Violin plot showing average expression levels of selected reactivity markers among mononuclear phagocyte populations.

(B) Frequencies of MG_1 and MG_2 subpopulations among total microglia between center and periphery. Symbols represent individual patients and paired samples are indicated by connecting lines. 3 of 4 (75%) paired samples showed an increased abundance of MG_1 cells in the tumor periphery and decreased frequency of MG_2 cells. Statistical significance was assessed by diffcyt-DA-voom method, *FDR corrected p value < 0.05.

(C) Volcano plot showing differentially expressed genes (FDR corrected p value < 0.05, indicated by blue and yellow) in CD4+ T cells from tumor periphery versus tumor center.

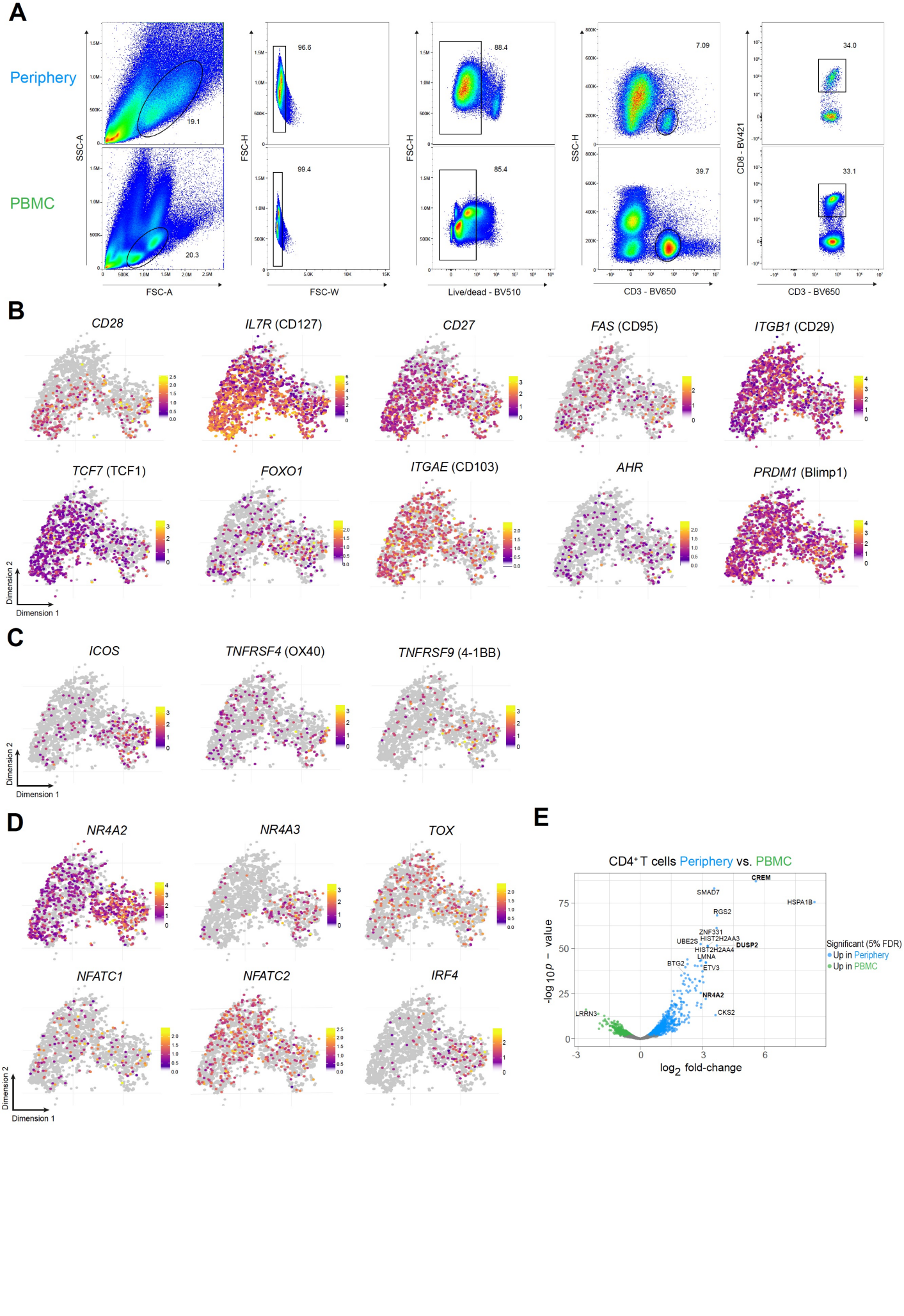
A
Periphery
PBMC
SSC-A
FSC-A
19.1
20.3
FSC-H
FSC-W
96.6
99.4
Live/dead - BV510
88.4
85.4
SSC-H
CD3 - BV650
7.09
39.7
CD8 - BV421
34.0
33.1
B
CD28
IL7R (CD127)
CD27
FAS (CD95)
ITGB1 (CD29)
TCF7 (TCF1)
FOXO1
ITGAE (CD103)
AHR
PRDM1 (Blimp1)
Dimension 1
Dimension 2
C
ICOS
TNFRSF4 (OX40)
TNFRSF9 (4-1BB)
D
NR4A2
NR4A3
TOX
NFATC1
NFATC2
IRF4
E
CD4⁺ T cells Periphery vs. PBMC
-log 10 p − value
log2 fold-change
CREM
SMAD7
HSPA1B
RGS2
ZNF331
HIST2H2AA3
UBE2S
DUSP2
HIST2H2AA4
LMNA
BTG2
ETV3
NR4A2
CKS2
LRRN3
Significant (5% FDR)
Up in Periphery
Up in PBMC

Figure S5. CD8$^+$ T cell phenotype is site-specific, related to Figure 5.

(A) Gating strategy for paired tumor-periphery and PBMC cells; after debris, doublet and dead cell removal, CD8+ T cells were identified as CD3+ CD8+ events.

(B-D) Single-cell expression of markers associated with naive/memory (CD28, IL7R, CD27, FAS, CD29, TCF, FOXO1) and tissue-resident memory (ITGAE, AHR, PRDM1) (B) T cell co-stimulation (C) and T cell exhaustion/dysfunction (D) overlaid on tSNE CD8+ T cell cluster.

(E) Volcano plot showing differentially expressed genes (FDR corrected p value < 0.05, indicated by blue and green) in CD4+ T cells from tumor-periphery versus PBMC.

A

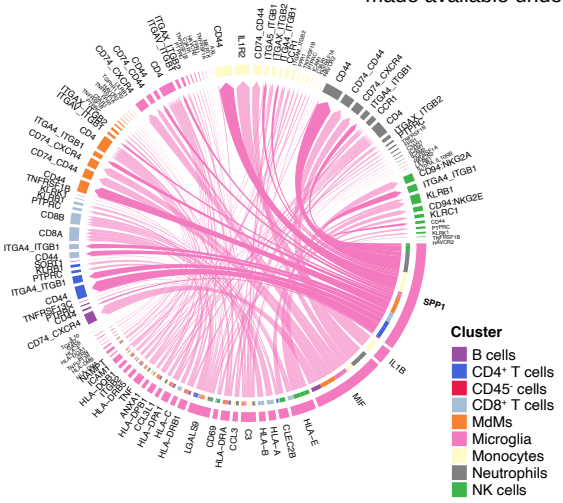

B

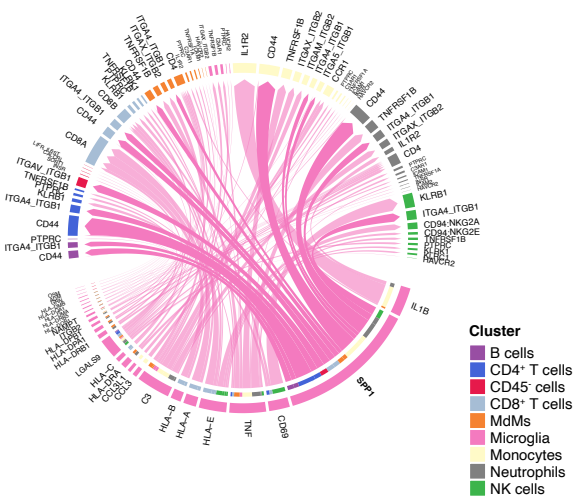

C

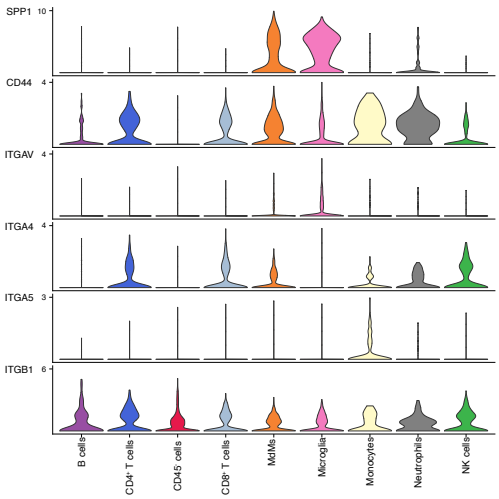

D

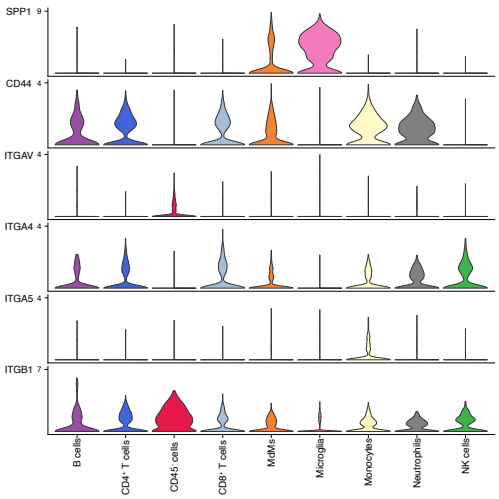

Figure S6. Cell-cell communication analysis using CellChat, related to Figure 6.

(A and B) Chord diagram showing significant interactions from microglia to all cell clusters in center (A) and periphery (B). The inner bar colors represent the targets that receive signal from the corresponding outer bar. The inner bar size is proportional to the signal strength received by the targets. Chords indicate ligand-receptor pairs mediating interaction between two cell clusters, size of chords is proportional to signal strength of the given ligand-receptor pair.

(C and D) Violin plots showing the expression distribution of signaling genes involved in the inferred SPP1 signaling network in center (C) and periphery (D).

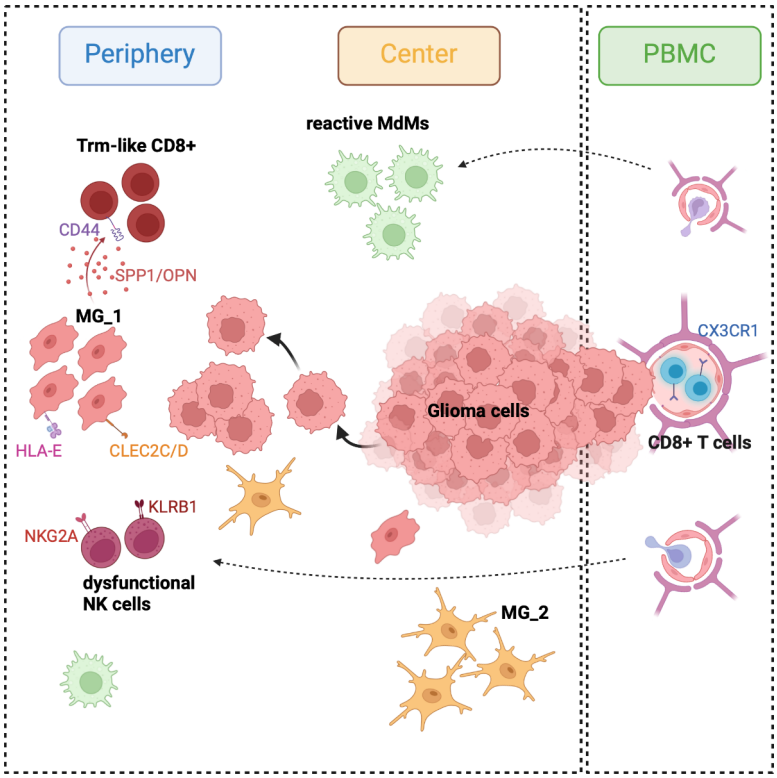

Figure S7. Graphical abstract. Proposed schematic of grade 4 glioma-associated immune cells in the three regional compartments. Created with BioRender.com.

Supplement References

1. Monaco, G., B. Lee, W. Xu, S. Mustafah, Y.Y. Hwang, C. Carré, N. Burdin, L. Visan, M. Ceccarelli, M. Poidinger, A. Zippelius, J. Pedro de Magalhães, and A. Larbi, *RNA-Seq Signatures Normalized by mRNA Abundance Allow Absolute Deconvolution of Human Immune Cell Types.* Cell Rep, 2019. **26**(6): p. 1627-1640.e7.

2. Klemm, F., R.R. Maas, R.L. Bowman, M. Kornete, K. Soukup, S. Nassiri, J.P. Brouland, C.A. Iacobuzio-Donahue, C. Brennan, V. Tabar, P.H. Gutin, R.T. Daniel, M.E. Hegi, and J.A. Joyce, *Interrogation of the Microenvironmental Landscape in Brain Tumors Reveals Disease-Specific Alterations of Immune Cells.* Cell, 2020. **181**(7): p. 1643-1660.e17.

3. Müller, S., G. Kohanbash, S.J. Liu, B. Alvarado, D. Carrera, A. Bhaduri, P.B. Watchmaker, G. Yagnik, E. Di Lullo, M. Malatesta, N.M. Amankulor, A.R. Kriegstein, D.A. Lim, M. Aghi, H. Okada, and A. Diaz, *Single-cell profiling of human gliomas reveals macrophage ontogeny as a basis for regional differences in macrophage activation in the tumor microenvironment.* Genome Biology, 2017. **18**(1): p. 234.

4. Neftel, C., J. Laffy, M.G. Filbin, T. Hara, M.E. Shore, G.J. Rahme, A.R. Richman, D. Silverbush, M.L. Shaw, C.M. Hebert, J. Dewitt, S. Gritsch, E.M. Perez, L.N. Gonzalez Castro, X. Lan, N. Druck, C. Rodman, D. Dionne, A. Kaplan, M.S. Bertalan, J. Small, K. Pelton, S. Becker, D. Bonal, Q.-D. Nguyen, R.L. Servis, J.M. Fung, R. Mylvaganam, L. Mayr, J. Gojo, C. Haberler, R. Geyeregger, T. Czech, I. Slavc, B.V. Nahed, W.T. Curry, B.S. Carter, H. Wakimoto, P.K. Brastianos, T.T. Batchelor, A. Stemmer-Rachamimov, M. Martinez-Lage, M.P. Frosch, I. Stamenkovic, N. Riggi, E. Rheinbay, M. Monje, O. Rozenblatt-Rosen, D.P. Cahill, A.P. Patel, T. Hunter, I.M. Verma, K.L. Ligon, D.N. Louis, A. Regev, B.E. Bernstein, I. Tirosh, and M.L. Suvà, *An Integrative Model of Cellular States, Plasticity, and Genetics for Glioblastoma.* Cell, 2019. **178**(4): p. 835-849.e21.